Fall 11-12-2022

The Impact of Contact Geometry on Sea Ice Stress and Fracture at the Scale of Ice Floes

Michael J. May
Dartmouth College, michael.j.may.th@dartmouth.edu

Recommended Citation

May, Michael J., "The Impact of Contact Geometry on Sea Ice Stress and Fracture at the Scale of Ice Floes" (2022). *Dartmouth College Master’s Theses*. 61.
https://digitalcommons.dartmouth.edu/masters_theses/61

The Impact of Contact Geometry on Sea Ice Stress and Fracture at the Scale of Ice Floes

A Thesis
Submitted to the Faculty
in partial fulfillment of the requirements for the
degree of

Master of Science

in

Engineering Sciences

by Michael J. May

Thayer School of Engineering
Guarini School of Graduate and Advanced Studies
Dartmouth College
Hanover, New Hampshire

July 2022

Examining Committee:

Chairman________________________
(Christopher Polashenski, Ph.D.)

Member_________________________
(Donald Perovich, Ph.D.)

Member_________________________
(Erland Schulson, Ph.D.)

____
F. Jon Kull, Ph.D.
Dean of the Guarini School of Graduate and Advanced Studies

(I will obtain this signature)

Abstract

Observations of stress and strain at the scale of ice floes are necessary to fill a gap in our understanding of sea ice mechanical behavior. Current climate and ice dynamics models represent ice mechanical properties using stress-strain relationships largely determined at laboratory-scale (<1m) or from regional-scale (10+km) deformation observations. The former scale does not include all mechanisms of deformation operating in the ice pack; the latter aggregates multiple modes of deformation into non-physical fluid analogies. The Sea Ice Dynamics Experiment (SIDEx) was run in Feb-Mar 2021 to fill this gap, observing stress and strain at the scale of sea ice failure processes. Here we present stress sensor observations. Stress gages (N=31) were deployed over a 4.5km^2 area in the southern Beaufort Sea to observe in-situ stress. These data were analyzed in the context of deformation observations from satellite imagery and local laser and radar interferometers to explain the drivers of sea ice stress variations before and after fracture. Three case studies between 14 March and 24 March, during which fractures propagated through the stress observing array, are presented here. We find that the contact geometry between floes, along with the regional motion that is driving the floes to interact, is consistent with the observed stress state, fracture, and orientation of stress post-fracture at local scale. When the floe is contiguous and fractures are far away, stress magnitude and orientation is similar across the entire domain and changes are highly correlated. As the floe fractures, spatial variability in stress increases and high stresses are found along the floe contacts. Peak stresses occur on or near contacting asperities, reaching up to 600 kPa, and along paths connecting contact points. The interrelation between stress state and geometry suggests that high fidelity models, initialized with realistic floe geometry, may have deterministic predictive capability for further ice fracture.

Acknowledgements

I would first like to praise and thank God, who has blessed me with the opportunity to study His glory in creation. His grace has sustained me through my time here and I stand in awe of His goodness.

I would like to thank my advisor, Chris Polashenski, for his continued support throughout my degree program. He has consistently challenged and mentored me, helping me build the skills and knowledge necessary to complete this thesis. I am deeply grateful for his guidance. Thank you also to Don Perovich. His knowledge of the field and rich research experience provided a great help to me in thinking through what my results meant. The conversations about golf helped me take a deep breath, too.

Thank you to the SIDEx team who worked with me on this project. A special thanks to Jenny Hutchings, Emily Fedders, Nick Wright, Pat Saylor, Matt Parno, Andy Mahoney, and Kelsey Kaplan who have worked closely with me this past year. This study is possible because of your efforts to plan, collect, and analyze this tremendous dataset. Thank you to the Thayer faculty who have taught and mentored me. A special thanks to Erland Schulson, Mary Albert, and Ron Lasky. Each of you have strongly impacted my time here in a unique way – I am grateful for your advice and your support.

Lastly, I would like to thank my parents and also my fiancé, Maddie. To Mom and Dad, it has been difficult to be so far away for so long. Thank you for understanding and for supporting me even though it has been hard. This degree is in celebration of you. To Maddie, thank you for loving me each day… and being patient with me as I forgot a few pieces of wedding planning here and there as I wrote this thesis. Second to Christ, you three are my pride, joy, and have my heart.

This thesis conveys results from the Sea Ice Dynamics Experiment, funded by the Office of Naval Research Code 32 Division 322 Arctic and Global Prediction Program. All GPRI figures are work completed by Emily Fedders, University of Alaska Fairbanks.

Table of Contents

Abstract ii

Acknowledgements iv

Table of Contents vi

List of Tables vii

List of Figures viii

List of Acronyms xi

1. Introduction 1

2. Background 3

3. Methods 9
  - 3.1 Stress Sensor Overview 12
  - 3.2 SIDEx Sensor Deployment 15
  - 3.3 Strain Measurements 24
  - 3.4 Satellite Imagery 25

4. Results 26
  - 4.1 Temporal Variability of Stress 26
  - 4.2 Spatial Correlation 31
  - 4.3 Fracture Period Analysis 34
    - 4.3.1 Pre-Fracture Period History 34
    - 4.3.2 Fracture Period 1: 14:30 – 17:30, 14 March 35
    - 4.3.3 Inter-FP 1: 17:30, 14 March to 12:00, 15 March 44
    - 4.3.4 Fracture Period 2: 12:00, 15 March to 01:00, 16 March 45
    - 4.3.5 Inter-FP 2: 01:00, 16 March to 01:30, 19 March 55
    - 4.3.6 Fracture Period 3: 01:30, 19 March to 06:00, 20 March 56
    - 4.3.7 Post-FP 3: 06:00, 20 March to 00:00, 21 April 65

5. Discussion 67

6. Conclusion 69

References 71

List of Tables

Table 1: VWSG deployment dates, positions, and installation orientation…………….. 16

Table 2: Temporal autocorrelation values for 10-day duration, with a case-study of a 3-day period from 12:00, 15 March to 12:00, 18 March………………………………… 30

Table 3: Correlation coefficients between sensors and between each sensor and the stress average ……………………………………………………………………………….. 32

Table 4: Average correlation coefficients for sensors on Camp ECW and Camp North ………………………………………………………………………………………... 32

List of Figures

Figure 1: SIDEx camp drift from 7 March 2021 to 19 April 2021…………………… 10

Figure 2: Overview of the VWSG installation location, with the Main Camp (yellow) and East Camp (red) positions highlighted.………………………………………………. 12

Figure 3: Stress vs. time without residual stress correction …………………………… 19

Figure 4: SIDEx data corrected assuming each wire spends 5% of time in tension ……. 20

Figure 5: SIDEx data corrected assuming each wire spends 12.5% of time in tension…. 20

Figure 6: SIDEx data corrected assuming each wire spends 20% of time in tension …. 21

Figure 7: Mohr-Coulombic failure envelope plotted as p vs. q ….……………………... 23

Figure 8: Mohr-Coulombic failure envelope plotted as σ_N *vs.* τ …………………… 23

Figure 9: Map of the LSO reflectors with the Main Camp (left) and East Camp (right) LSO scanners marked in red.……………………………………………………………. 25

Figure 10: Temporal autocorrelation from 14 March to 24 March ………………...…… 29

Figure 11: Temporal autocorrelation from 12:00, 15 March to 12:00, 18 March ……… 29

Figure 12: Temporal autocorrelation during FP 2 ……………………………………… 30

Figure 13: Temporal autocorrelation during Inter-FP2, from 06:00, 17 March to 12:00, 18 March ……………………………………………………………………………… 30

Figure 14: Correlation between the ice thickness and average stress at each site….…... 34

Figure 15: RadarSAT image taken on 15:50, 13 March with features highlighted. Motion arrows indicate motion relative to the camp center point, the entire field of view is also moving WNW. Shear can be seen by relative displacement of components of the three zones…………………………………………………………………………….. 36

Figure 16: Cosmo-SkyMed image taken on 16:02, 16 March. Ice movement is noted by blue arrows………………………………………………………………………... 37

Figure 17: Regional context around the Camp Floe at 22:38, 13 March……………… 38

Figure 18: East and west contact points at 14:49, 14 March…………………………... 39

Figure 19: East contact point at 14:49, 14 March……………………………………….. 39

Figure 20: Crack displacement visualized in Cosmo-SkyMed SAR imagery on 04:21, 15 March……………………………………………………………………………… 40

Figure 21: GPRI interferograms calculated between 15:15 and 15:30……………...... 41

Figure 22: GPRI interferograms calculated between 15:30 and 16:00………………….. 41

Figure 23: Stress change from 15:58 to 15:59, 14 March……………........................... 42

Figure 24: Stress vs. time during FP 1……….. 44

Figure 25: Stress vs. time during Inter-FP 1……………………………………………. 45

Figure 26: Crack positions in the Camp Central and Camp East floes from a 21:47, 16 March WV image…………………………………………………………………… 47

Figure 27: GRPI interferogram calculated from 16:52 to 17:04, 15 March…………… 48

Figure 28: LSO reflector movement from 16:55 to 17:06, 15 March ………………..…. 48

Figure 29: Stress change from 16:43 to 16:50, 15 March.………………………………. 49

Figure 30: Timeseries stress record of FP 2 with an inset of the FP 2 initial fracture…... 49

Figure 31: Stress change from 22:33 to 22:37, 15 March……………………………….. 51

Figure 32: Stress vs. time of FP 2 with an inset of the 22:34-23:40 series of stress events ……………………………………………………………………………………... 52

Figure 33: LSO reflector movement from 22:13 to 22:54, 15 March…………………… 53

Figure 34: Stress change from 22:55 to 22:59, 15 March……………………………….. 54

Figure 35: Stress change from 22:59 to 23:03, 15 March…………………………...….... 55

Figure 36: Stress vs. time during Inter-FP 2…………………………………….…... 56

Figure 37: MODIS image of Southern Beaufort Sea on 21:55, 14 March……………… 57

Figure 38: MODIS image of Southern Beaufort Sea on 06:30, 18 March.…………..…. 58

Figure 39: Aerial structure-from-motion image of floe deformation and cracks on 20 March ……………………………………………………………………………… 59

Figure 40: GPRI interferogram calculated from 04:08 to 04:14, 19 March………...….... 60

Figure 41: Stress change from 04:09 to 04:10, 19 March……………………………….. 60

Figure 42: GNSS record of buoy position change during FP 3…………………………. 62

Figure 43: Stress release between 17:35 and 17:36, 19 March………………………… 63

Figure 44: Stress vs. time of FP 3 with an inset around the 17:35 stress event………… 64

Figure 45: Stress change from 20:48 to 20:49, 19 March……………………………...... 65

Figure 46: Stress vs. time from the end of FP 3 to the conclusion of the experiment on 21 April…………………………………………………………………………….. 66

List of Acronyms

Sea Ice Dynamics Experiment	SIDEx
Sea Ice Mechanics Initiative	SIMI
meter-to-kilometer	m-km
Coordinated Eastern Arctic Experiment	CEAREx
multi-year	MY
first-year	FY
Surface Heat Budget of the Arctic Ocean	SHEBA
Vibrating Wire Stress Gage	VWSG
GAMMA Portable Radar Interferometer II	GPRI
Laser strain observer	LSO
Maxar-Digital Globe Worldview	WV
RADARSAT Constellation Mission	RCM
Center for Southeastern Tropical Advanced Remote Sensing	CSTARS
Dynamically active periods	DP
Low dynamic activity periods	LP
Fracture Period 1	FP 1
Fracture Period 2	FP 2
Fracture Period 3	FP 3
Power Index	PI
Camp East, Central, and West Floes	Camp ECW

1. Introduction

Climate change has caused rapid sea ice decline in the Arctic, resulting in a weaker and thinner ice cover [1]. Models of sea ice are critical to understanding, operating in, and predicting this changing environment. One of the most important, but challenging, ice processes to represent is deformation. Ice deformation is currently modeled using nonphysical fluid analogies [2] and/or physically based parameterizations determined from laboratory fracture tests [3] to relate stress and strain. Significant observational evidence suggests the parameterizations used in current models are non-representative in important ways [4]. Further observations are needed to improve these parameterizations. Past studies have resolved the stress-strain-fracture behavior of ice at the sub-m scale [5] and at scales greater than 10 km [6]. Laboratory studies have led to a prevailing hypothesis that internal flaws are responsible for in-situ ice having a lower observed compressive strength than laboratory ice [3], [7], [8]. This is hypothesized to hold at the meter-to-kilometer (m-km) scale based on crack geometries observed in the field [9]. No study to date has assessed how contact geometry affects fracture at this scale through contemporaneous stress-strain measurements. We hypothesize that floe contact geometry, and the resulting stress concentrations, are responsible for most fractures observed in Arctic pack ice.

The Sea Ice Dynamics Experiment (SIDEx) was conducted in the Beaufort Sea from Feb-Mar 2021 to fill this knowledge gap. Using recent advances in satellite remote sensing, high-precision GNSS, and interferometric rangefinders, the project deployed a high-resolution stress and strain-observing array on a mixed multi-year and first-year ice floe. The SIDEx goal is to resolve the stress-strain-fracture of sea ice in a real heterogeneous ice floe, improving modeling capabilities by better constraining the drivers of fracture. The internal stress state and floe-floe interactions were continuously monitored over a roughly 49-day period between 3 March and 21 April. This paper focuses on the stress data from the experiment. An array of 31 in-situ stress sensors, deployed over a 4.5 km^2 area, was used to resolve the spatial and temporal variability of stress.

We focus our analysis on explaining the transfer of stress between floes during kinematic interactions and the propagations of stress across a heterogeneous, multi-floe ice cover. Three case studies from 14 March to 20 March featuring known fracture events are analyzed to understand sea ice mechanical behavior. Special attention is given to how internal stress pathways are governed by the contact geometry between floes. Satellite imagery of the region gives context to the far-field stress and local deformation observed over a given time. Radar and laser interferometers observe fracture initiation, propagation, and/or displacement. This local ice movement is combined with stress data to determine failure modes and the general mechanical behavior of the floe.

The overarching goal of this study is to better constrain sea ice mechanical behavior at the m-km scale for the purpose of improving ice dynamics models. The specific goal of this study is to better understand the temporal and spatial variation in stress, and how this is impacted by floe-floe interaction and contact geometry between floes. Details on the stress sensor used, deployment strategy, strain array, and satellite imagery used are detailed in the Methods section. The temporal variability of stress, spatial correlation of stress, and case study analysis of three events are presented in the Results section. Lastly, we discuss stress pathways in ice, geometric stress concentrations, crack propagation, and failure modes in ice.

2. Background

Past studies have used in-situ stress sensor arrays to understand stress variability and how stress is transferred through the ice. Since stress cannot be measured directly, many studies have estimated in-situ stress by determining the strain of an elastic inclusion embedded in the ice. Several sensors were created in the mid-20th century to measure ice stress in this way. Cox and Johnson (1983) reviewed these sensors and determined two superior designs [10]. The first was a stiff cylindrical inclusion that would measure biaxial stress by determining the radial deformation of the cylinder wall in 3 directions, and the second was a thin, wide sensor that would have an effective modulus like that of ice. They then presented the theory for determining stresses from the stiff cylindrical sensor which prompted later studies to use that sensor type, including our own.

These sensors were field tested in the spring of 1984, when 18 of these biaxial stressmeters were deployed at 6 sites near Esso' caisson retained island in Mackenzie Bay, Canada [11]. Sensors were installed at 30, 80, and 130cm depths at each of the 6 sites to assess the through-thickness variability of sea ice stress. The authors found a heterogeneous stress profile, with vertical and horizontal variability. Maximum peak stresses were observed at each level of the ice at different times, differing from the expectation that only the top layer of ice would experience the highest stresses. The authors proposed that the variability in vertical stresses suggests a bending of the ice sheet. Stresses also varied horizontally across the ice and were seen to increase directionally from west to east, which the authors speculated is due to the presence of grounded MYI to the east. This study established that stresses in ice are highly variable, dependent on many factors such as temperature and ice thickness distribution.

The horizontal and vertical distribution of ice stress was further explored by Tucker and Perovich during the Coordinated Eastern Arctic Experiment (CEAREx) in Fall 1988 [12]. VWSGs were installed at 2 multi-year (MY) floes. At site 1, the vertical distribution of stress was investigated with 3 sensors being installed at depths 0.25, 0.70, and 1.20m within a 1.60m thick floe. This site was approximately 200 m from the floe edge. At site 2, the horizontal distribution of stress was investigated with 3 sensors (a, b, c) installed in a straight line at depths between 0.20 and 0.25m. The site spanned a MY and first-year (FY) ice boundary, with sensor A being 7m from the boundary in the FY zone, and sensor B and C being 2 and 15m from the boundary in the MY zone, respectively. The FY ice thickness at sensor A grew from 0.38 to 0.54m during the experiment and the MY ice thickness at sensors B and C was 2m.

Tucker and Perovich found that the relationship between stresses observed at different levels of the ice varied. During one event the VWSGs installed at mid- and lower-depth recorded stresses near 50 kPa while the top layer VWSG recorded a 90 kPa stress. This finding, that the sensors at depth were experiencing only ~60% the stress of the top layer, was expected by previous evidence that mid-depth stress was about half that observed in the upper quartile depths [13]. 2 weeks later, however, the sensors recorded a dynamic event with a vertical stress profile of different character. Here, the top sensor recorded a maximum of 130 kPa while the mid-depth sensor recorded a maximum of 150 kPa. The authors speculated that the difference is due to contact geometry, with thin FY ice loading the top of the floe during the first event and thick MY ice in contact with the floe at mid-depth during the second event.

Large horizontal variations of ice stress were also found. The most frequent occurrence of high stress events occurred near the floe edge. The stress at the edge of the MY ice tended to be well correlated with the nearby FY ice stress, but poorly correlated with the other MY ice stress location 13m away. The sensor 15m from the floe edge had a correlation of 0.82 with the FY ice but experienced stresses approximately 17% of the FY ice values. Nevertheless, it was the 15m MY ice location that experienced the highest peak stress, recording a 460 kPa event. This result calls attention to the complex stress pathways found in sea ice. There was also evidence of stress attenuation. The stress sensors at site 1, 200m from the edge site, recorded consistently lower stresses than the sensors near the edge. This led the authors to hypothesize that stresses recorded far from the edge represent spatially averaged pack ice stress, which could be used in large-scale dynamics models, while those closer to the floe edge represented the concentration of stresses due to contact geometry. In both the vertical and horizontal stress profile, contact geometry was a primary factor in describing variability.

The stress data attained by Tucker and Perovich were the first test data in a new model that began accounting for sea ice anisotropy, including ridges and leads [14]. To gather the necessary stress and strain data to better validate the model, the Sea Ice Mechanics Initiative (SIMI) had a field campaign from Fall 1993 to Summer 1994. Richter-Menge and Elder (1998) present the stress results from this campaign [15]. Here, stresses were monitored at one center site and three edge sites of a MY floe over six months in the Beaufort Sea. 7 VWSGs were deployed in MY ice at each edge site at an average depth of 22.1cm. Sensors were installed in a line to determine attenuation from the edge. One sensor site remained intact for the duration of the campaign and provided useful data.

The authors note that the largest difference between the stress signals came in the high-frequency component. Periods of high-frequency activity would peak between 50 and 100 kPa on the floe edge. An interesting finding was that site 1, which had to be relocated 400m back due to large deformation events, typically peaked between 100 and 200 kPa. In all cases, stress would attenuate towards the center of the floe. The center site stayed below 50 kPa for most of the campaign, experiencing primarily thermal stresses during the experiment. Such attenuation, however, was not found over a 13m distance, differing from the findings of Tucker and Perovich.

To explain the difference, Richter-Menge and Elder compared SIMI observations to finite-element model results of the CEAREx campaign from Frederking and Evgin [16]. Richter-Menge and Elder found that the contact geometry of the SIMI floe caused the load to be applied over a much broader area, leading to a more homogenous near-edge stress profile than Tucker and Perovich experienced.

A diurnal thermal signal was present in the stress record. Thermal stresses were found to be isotropic and impacted stress measurements between 15-20 kPa°C^{-1}. The authors note that the correlation between the secondary principal stress and the ice temperature was strong at every site, ranging from 0.80 to 0.86. The primary principal stress was less correlated with ice temperature, ranging between 0.30 and 0.72. The more high-frequency stresses were recorded, the less a site's primary principal stress tended to be correlated with ice temperature. Since the minor principal stress maintained a high correlation irrespective of high-frequency events, the authors proposed that the dynamic stresses, or those caused by ice-motion, can be approximated by subtracting the minor principal stress from the major principal stress.

Richter-Menge and Elder note that dynamic events appear to occur on the timescale of minutes instead of days. They also note that high-frequency oscillations are at times superimposed over an increasing signal. They argue that this behavior shows the continued loading and subsequent local failure of weaker ice. As weaker ice in contact with a loading body fails and ridges, the pack becomes stronger as thicker ice takes more load, and the stress progressively increases. This process of 'strain hardening' continues until little to no weak ice remains and the internal stress reaches the failure strength of MY ice, resulting in ridge building of the strongest ice. This theory of ice displaying a type of hardening behavior was expounded on in another study [17], which approximated ice behavior as a granular plastic by observing sea ice kinematics using drifting buoys and SAR imagery. A necessary step to validating this finding was to link in-situ stress observations to regional scale deformation to assess the correlation between the two. This was one of the primary objectives for the dynamics component of the Surface Heat Budget of the Arctic Ocean (SHEBA) experiment that ran from 1997 to 1998.

During SHEBA, Richter-Menge, McNutt, Overland, and Kwok conducted an experiment relating ice stress and deformation at the regional scale [18]. They deployed 8 VWSGs over a ~15x15km area ~500km off the Alaskan coast in the Beaufort Sea. Sensors were installed at an average depth of 39cm in ice with an average thickness of 130cm. 6 sensors were installed on the main SHEBA floe, 5 of which were installed in a straight line spaced 1 km apart. The final SHEBA sensor was installed further towards the floe center near the midpoint of the sensor line. The other two sensors were installed on individual floes approximately 15 km from the SHEBA station. The sensors were operational from 15 October 1997 through 1 April 1998. Ice motion products from satellite imagery tracked regional deformation and were used in qualitative assessments of specific events. The authors used 4 unique case studies to describe the interrelation between regional deformation and internal ice stress.

To assess the dynamic response of the ice, the authors employed the technique used to analyze the SIMI data [15] and approximated the ice-motion-driven stress by subtracting the secondary principal stress from the primary principal stress. A correlation analysis was run for the array to determine the spatial relationship between sensors. Correlation between sites ranged from 0.07 to 0.67, with an average value of 0.36 +/- 0.15. The correlation between each site and the stress average across all sensors was higher, being an average 0.65 +/- 0.14. The authors concluded, therefore, that the all-sensor stress average was the best representation of regional-scale ice stress.

The authors analyzed stresses during times of regional ice convergence, divergence, and granular behavior over the course of SHEBA. They conclude that internal ice stress is related to regional ice deformation. The hardening theory posed by Richter-Menge and Elder, that progressive ice strengthening occurs through the elimination of weaker ice through compression events, was advanced in this study. A progressively increasing, quickly fluctuating stress signal was seen during times where southernly winds were compacting the ice up against the coast. These would last until the westerly winds returned and the ice resumed its westward drift, nearly eliminating the internal ice stress. Ice stress was also dependent on location. Southward winds would increase ice stress if the Alaskan coast was to the south. Once the westward drift pushed the SHEBA camp beyond Point Barrow, no compaction happened; the Chukchi ice remained unconsolidated on shore. Thus, no stress built up. The authors pose 3 general rules for ice stress to build up in the Beaufort Sea during winter. First, there must be a fully formed ice cover connecting MY ice to the Alaskan coast. Second, there must be sufficient wind. Third, this wind must be pushing ice towards the coast [18]. The stress increase continues until the FY ice is eliminated and the thick MY ice eventually fails. This linking of stress to the regional context in a detailed, qualitative way was the first of its kind. The data was used to further develop a seminal discrete-element model [19] that better enabled modelling of heterogenous Arctic pack ice.

Each of these studies shed new light on the mechanical behavior of sea ice, and how stress builds up and propagates through pack ice. Stress variability observed in early studies led researchers to install in-situ sensors at various depths and horizontal spatial resolutions, culminating in the SHEBA effort to link stress to regional-scale deformation. The next relationship that must be defined is how stress observations are linked to local deformation. In each study, an analysis of local deformation is either omitted, treated as an aggregated feature of larger-scale deformation, or is inferred based on stress behavior. Our study offers the first comprehensive view of local stress-strain-fracture, continuing to build an observational understanding of sea ice mechanical behavior.

3. Methods

Observations were collected at the Sea Ice Dynamics Experiment (SIDEx) drifting ice camp, situated on a mixed multi-year (MY) and first-year (FY) ice floe in the

Southern Beaufort Sea during late winter and early spring 2021. The camp itself was established near a large MY pressure ridge on a small (~100m diameter) fragment of heavy (5m+ thick) MY ice in a region of mixed MY and FY ice. Camp center was located at 71.021°N, 143.905°W at 18:15 UTC, 3 March and drifted approximately 260 km to 71.803°N, 150.737°W by time 15:00, 23 April, when most observations were discontinued (Figure 1).

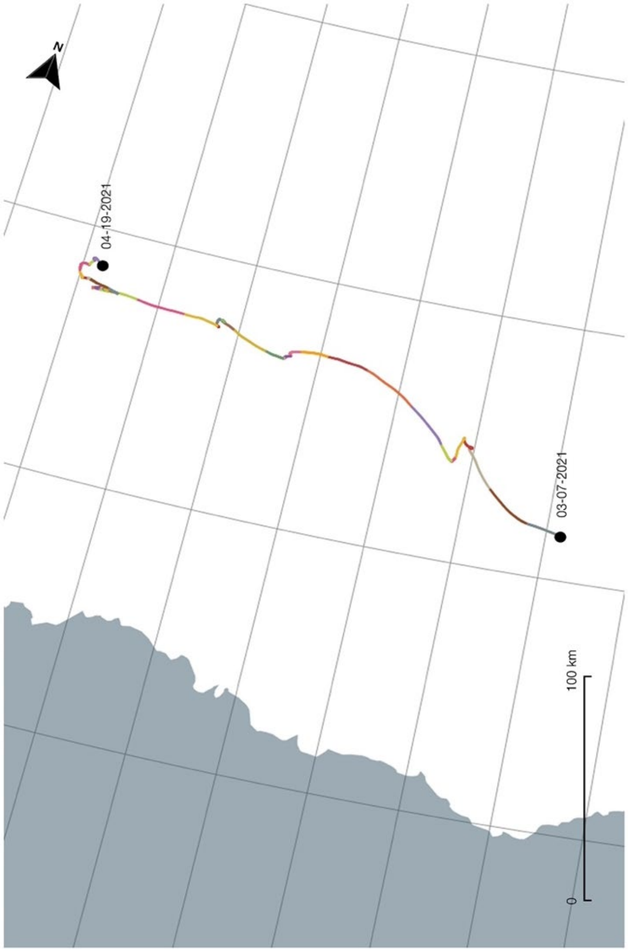

Figure 1. SIDEx camp drift from 7 March 2021 to 19 April 2021.

On-ice personnel occupied the camp from 3 March 2021 through 19 March 2021 and installed an instrument array designed to observe stress, strain, and fracture in the sea ice at meter-to-kilometer (m-km) scale. Installation of the array was generally complete on 13 March. Multiple sensor types were deployed, including in situ stress gauges, laser and radar strain observing systems, a seismo-acoustic fracture detection system, single and dual frequency GNSS buoys, and a meteorological station. This paper focuses on results from the stress gauges. To aid in interpretation of the results, surveys of ice and snow thickness were also made and multiple types of aerial imagery and tasked satellite remote sensing imagery were collected. These included sub-meter resolution optical imagery (airborne imagery, Maxar-Worldview (WV) and Planet-SkySat (PSS)) and synthetic aperture radar (RADARSAT Constellation Mission (RCM), TerraSAR-X, and COSMO-SkyMed). These provide additional context for the large-scale ice movements that are used with the stress-strain sensor arrays to draw failure hypotheses in this study.

The time history of the ice floe was fortuitous for the purposes of this experiment: Prior to our arrival, ice movement in the Beaufort Sea all but ceased for ~2 weeks under weather conditions of calm winds and cold temperatures (-50 to -30C). Though the ice floe selected had certainly experienced many prior deformation events, leaving it fractured and ridged, this meant that the ice floe was substantially re-bonded and contiguous at the start of our observations, containing no visible open fractures and no apparent recently worked ridges. All cracks or leads examined had refrozen to a thickness exceeding 90cm, suggesting they were about a month old. Ice motion resumed on 4 March. The first local lead or ridge formation was observed on 14 March and progressive failure of the ice floe fragmented it into a large number of pieces by late on 19 March (Figure 2), to a point which necessitated removing personnel from the floe. Hence our experiment observes the progressive fragmentation of an initially contiguous (though certainly heterogeneous) ice floe under stress: potentially an ideal experiment for understanding the mechanics of ice failure.

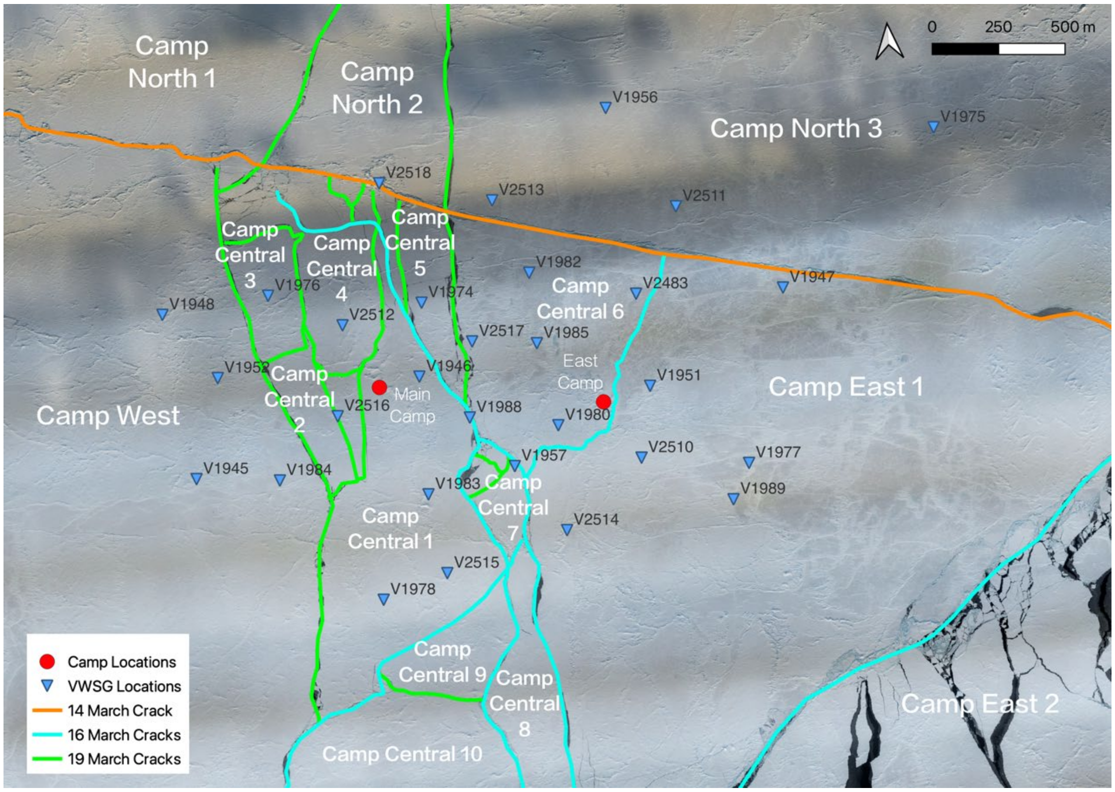

Figure 2. Floe map of the region surrounding the SIDEx Main Camp on 20 March. The map background is an Airborne Structure-from-Motion image, acquired by Matt Nolan.

3.1. Stress Sensor Overview

In-situ sea ice stress was observed using an array of 31 Geokon Model 4350 Biaxial Stressmeters [20]. The installation was configured to observe the spatial variability in ice stress across ice of heterogeneous character. The type of instruments used, commonly referred to as Vibrating Wire Stress Gages (VWSG), have been a primary instrument for assessing sea ice stress in Arctic sea ice over the last four decades [12], [15], [21], [22]. The Geokon Model 4350 VWSGs used are hollow steel cylinders measuring 31.75 cm long and 6cm in diameter. The VWSGs determine point stress by recording strain on the steel cylinder. Cylinder deformation is determined based on changes in the resonant frequency of three steel wires strung in tension across the hollow center of the cylinder, and arranged in the horizontal plane at 120° to each other. The wires are magnetically 'plucked' once per minute and their resonant frequencies are recorded using Campbell CRVW3 dataloggers [23].

Gages are installed with the cylinder long axis situated vertically, such that the sensors measure stresses only in the horizontal plane. We deployed all gages with their sensing plane at approximately 25 cm beneath the ice surface. The choice of a uniform deployment depth uses our limited number of sensors to assess horizontal stress variability, as opposed to vertical stress variability. Prior experiments have investigated vertical profiles of stress by deploying sensors in different horizontal planes. These have generally found high coherence between the stress changes seen at different levels of a single site, with the largest stresses seen near the surface [12]. Since the surface ice is also the coldest part of the ice at this time of year, it is likely also the stiffest and most brittle. We therefore presume that failure initiates in the high stress, brittle near-surface and observing there will provide the most accurate assessment of the stress conditions at failure, as well as the best signal to noise ratio.

Stress is calculated from the observed wire resonant frequencies using the method of Cox and Johnson [10]. This method converts changes in wire resonant frequency to wire displacement (eq. 1), then resolves the wire displacements into primary [p] and secondary [q] principal stresses (eq. 2 and 3). An angle is then calculated from the primary principal stress direction to the center wire V_{r1} (eq. 4). These are accomplished by relating current frequency measurements to a calibration curve determined from predeployment tests, which determined the response of each sensor to pressure. Since temperature changes of the sensor also induce thermal expansion or contraction of the wires and the gage, displacements are corrected for temperature, observed within the gage, prior to applying these calculations (eq. 5).

$$V_{r,i} = G_i\left(f_{0,i} - f_{T,i}\right) * \frac{1}{39};\ i = 1, 2, 3 \tag{1}$$

$$p = \frac{1}{2}\left[\frac{1}{3B}\left((2V_{r1} - V_{r2} - V_{r3})^2 + 3(V_{r2} - V_{r3})^2\right)^{1/2} + \frac{1}{3A}(V_{r1} + V_{r2} + V_{r3})\right] \tag{2}$$

$$q = \left[\frac{1}{3A}(V_{r1} + V_{r2} + V_{r3}) - p\right] \tag{3}$$

$$\theta = \frac{1}{2}\cos^{-1}\left[\frac{V_{r1} - A(p+q)}{B(p-q)}\right] \tag{4}$$

$$\varepsilon\ell(T_T, R_T) = \left[(R_0 - R_T) + K(T_T - T_0)\right]G \tag{5}$$

Here V_{r1}, V_{r2}, and V_{r3} are the wire displacements in μm, with V_{r1} being the center wire displacement. A and B are inclusion factors for the steel sensor embedded in the ice. f_0 and f_T are the wire frequencies at installation and at the new temperature, respectively, in s^{-1}, T_T is current temperature, and T_0 is the temperature at installation in Celsius. R_0 and R_T are the wire frequency readings at the initial and current times, respectively. $\varepsilon\ell$ is the radial wire displacement due to temperature, with ε being wire strain and ℓ being wire length. K is the thermal gage factor that denotes the resonant frequency change at each wire per degree Celsius temperature change, and G is the radial gauge factor that denotes the change in length per change in resonant frequency at each wire. Each is determined by calibration tests in a controlled pressure chamber prior to deployment. The inclusion factors account for the difference in elastic modulus between the stiff sensor and the surrounding ice; they are experimentally determined ratios of the undisturbed ice pressure to the pressure felt by the sensor, which necessarily creates some local stress concentration [10]. The stress orientation relative to the center wire strain is calculated as the clockwise angle from the primary principal stress to the direction of the center wire in Eqn. 3. This is required for a spatial analysis of stress and is used throughout our results and discussion to show direction of stress alignment. While the sensors are nominally rated by Geokon to have a maximum resolution of 14 kPa [20], the utilization of a superior data-logging system, such as our use of the Campbell CRVW3 dataloggers, has been shown to increase resolution to around 5 kPa for loads between 0 and 2 MPa [12], [21].

The VWSGs were calibrated for absolute readings using the method described in Cox and Johnson. A range of radial loads were applied to each gauge at several temperatures and the wire resonant frequencies were recorded under these loads. The observed readings were used to determine a sensor-specific calibration curve that was used to determine stresses from the wire strains. This calibration was completed prior to the field experiment by Geokon.

3.2 SIDEx Sensor Deployment

Each of the 31 VWSGs were deployed at the SIDEx field site using a method similar to that presented in Richter-Menge and Elder [15]. An ice auger was used to drill 8 cm diameter holes in the ice to a depth of ~50cm. The VWSG was oriented perpendicular to the surface within the hole and frozen into place at the depth such that the sensing rosette was 25+-2 cm beneath the ice surface. In the case of this experiment, holes were not drilled through the ice entirely and fresh water was used to fill the hole and freeze the sensors into place. We have found that the use of sea water in nonthrough-thickness holes frequently leaves large brine pockets near sensors, impacting ice coupling and the integrity of readings. Temperatures were sufficiently cold that we were able to manually hold the gages at the desired depth and orientation for a few minutes until they froze into place, avoiding the use of the PVC pipe and crossbar system used in prior experiments [3]. We have found the PVC pipe mounted to the stress gage and protruding up into the air wobbles on windy days and adds noise to stress readings and recommend against this particular prior deployment method. Each sensor was connected to a logger box by a cable, and the box was left on the ice surface and buried in snow to restore the original snow depth. The installation process was repeated for all 31 VWSGs.

The sensors were located within a roughly 4.5 km^2 area around the SIDEx camp, hereafter referred to as the Main Camp, deployed in a manner to sample spatial variability in stress state spanning a FYI-MYI boundary. Deployment sites were selected to be in areas where ice conditions were largely undeformed and uniform for at least a 10m radius around the installation site. No gages were deployed in deformed ice or unconsolidated blocks. Ice characteristics otherwise varied across deployment sites. Ice thickness was highly variable, ranging from 103 to 362 cm in the deployment sites. The VWSGs were installed with V_{r1} oriented towards magnetic North using a compass, or toward the GPRI at camp center visually, with their orientation recorded. Orientation was accurate to ~+/- 5 degrees. The output data was transformed to be relative to true north for all sensors, to facilitate inter-comparison between gages and other data sources. 30 of the 31 VWSGs successfully collected data over the course of the fracture events discussed in this paper, with V1981 being the lone defective sensor.

Sensor ID	Lat	Lon	Time	Install Direction

1946	71.02088	-143.901675	2021-03-03T12:18	Magnetic North
1988	71.01936	-143.896577	2021-03-03T12:25	Magnetic North
1957	71.017585	-143.89211	2021-03-03T12:47	Magnetic North
1980	71.018907	-143.887215	2021-03-03T12:59	Magnetic North
2516	71.019692	-143.91061	2021-03-03T15:20	Magnetic North
2512	71.022828	-143.909512	2021-03-03T15:52	Magnetic North
1974	71.023443	-143.900956	2021-03-03T16:05	Magnetic North
2517	71.021996	-143.895831	2021-03-03T16:26	Magnetic North
1951	71.020087	-143.877195	2021-03-03T18:23	Magnetic North
2483	71.0233	-143.87808	2021-03-03T17:43	Magnetic North
1985	71.0218	-143.888955	2021-03-03T18:01	Magnetic North
2510	71.01762	-143.878573	2021-03-03T18:38	Magnetic North
1983	71.018632	-143.904915	2021-03-04T10:09	Magnetic North
1987	71.015455	-143.911289	2021-03-04T10:31	Magnetic North
1984	71.020264	-143.922096	2021-03-04T10:57	Magnetic North
1952	71.024123	-143.928814	2021-03-04T11:10	Magnetic North
1976	71.027103	-143.92396	2021-03-04T11:24	Magnetic North
2518	71.031211	-143.913489	2021-03-04T11:44	Magnetic North
2513	71.031032	-143.903742	2021-03-04T12:06	Magnetic North
1982	71.036975	-143.943072	2021-03-04T15:02	Magnetic North
2511	71.040332	-143.935101	2021-03-04T15:25	Magnetic North
1947	71.03873	-143.932602	2021-03-04T15:48	Magnetic North
1977	71.034863	-143.949588	2021-03-04T16:20	Magnetic North

2515	71.03285	-143.9896	2021-03-04T16:38	Magnetic North
2514	71.035961	-143.987321	2021-03-04T17:04	Magnetic North
1989	71.473684	-146.22745	2021-03-09T17:20	GPRI
1975	71.481842	-146.221138	2021-03-09T14:40	GPRI
1981	71.486102	-146.218847	2021-03-09T17:54	GPRI
1956	71.487393	-146.229474	2021-03-09T18:09	GPRI
1945	71.489732	-146.361792	2021-03-10T11:25	GPRI
1948	71.497377	-146.367242	2021-03-10T11:47	GPRI

Table 1. VWSG deployment dates, positions, and installation orientation.

Post-processing the VWSG data requires assumptions to be made regarding what is considered zero dynamic stress. While it is readily apparent from the calibration when the steel cylinder is experiencing no stress, this is likely not equivalent to the surrounding ice experiencing no dynamic stress. The principal challenges are accounting for the stress already in the ice at the time of deployment, particularly thermal stress, which is relieved immediately around the sensor by the drilling/installation, and the stress created locally during sensor freeze-in as expansion of water during solidification results in high stress immediately around the sensor. The installation process, therefore, creates sensor readings not reflective of the surrounding ice state until several days or weeks later when creep relieves the local stress gradients. It is necessary to adopt a method to correct the data to a uniform baseline stress. If the ice were under no stress, it would be simple to wait until the observed stress had approached zero before considering measurements usable. Unfortunately, thermal and dynamic stresses were already in place and continue to evolve across the time period that freeze-in and pre-existing stresses relax. All methods we are aware of for implementing the re-zeroing correction are imperfect and we have lower confidence in the absolute stress than in the relative stress changes from one time to the next, which are resolved with high accuracy.

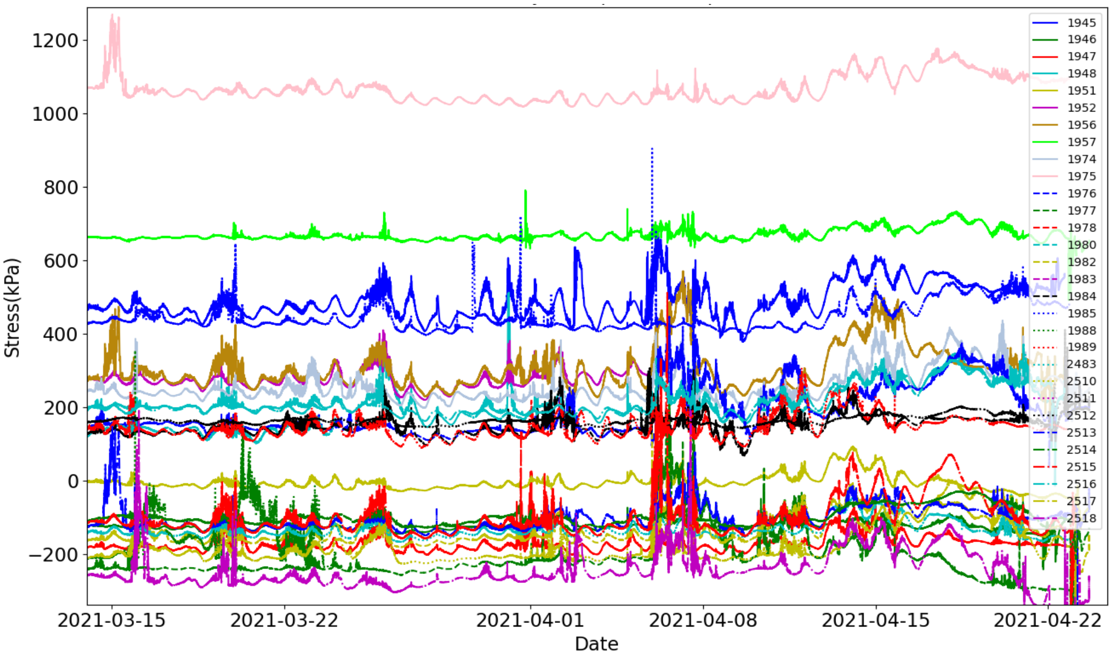

Figure 3. Stress vs. time without residual stress correction.

A common approach used by prior authors to re-zero sensors has been to visually select two “zero stress” times at the beginning and end of an experiment to calculate a linear fit and remove this from the stress record[12], [21]. Richter-Menge and Elder chose to use the wire readings at 0 kPa, 0°C at the beginning and end of the field experiment and apply a linear fit to that data, defining the time of 0 kPa readings as a period with no ice motion and no significant temperature change. We employ a slightly more sophisticated method, which reduces the absolute stress dependence on the particular zero-stress points selected. Instead of two points, it relies on the presumption that sensors return to a state of zero dynamic stress many times across the record and spends a significant percentage of time at this modal stress state. Here we use the 20th percentile stress, effectively assuming the ice spends 20% of time at stresses below this (i.e. in tension). Sites will likely spend more or less time in a state of tension, but since a significant amount of time is spent at the modal stress, the determined modal zero point is not particularly sensitive to the threshold chosen. Visual analysis of the data confirms that our chosen percentile approximates the line of most frequent stress.

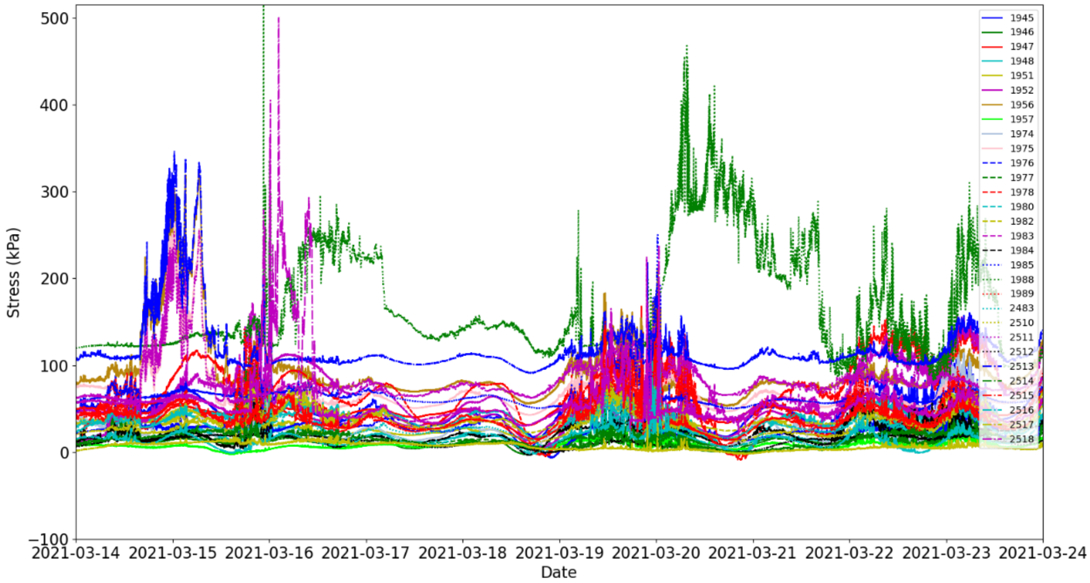

Figure 4. SIDEx data corrected assuming each wire spends 5% of time in tension

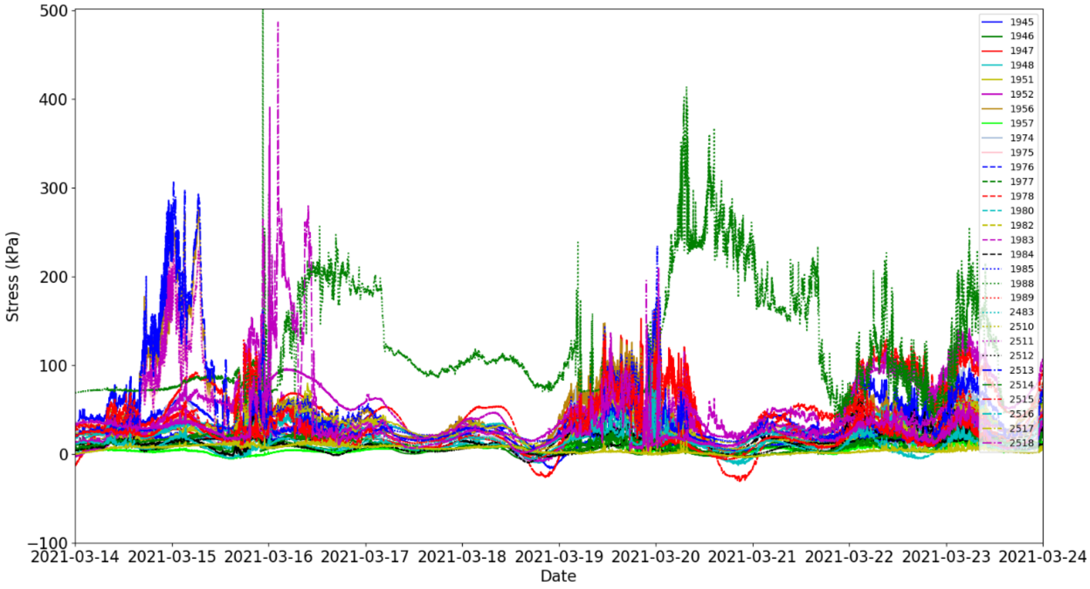

Figure 5. SIDEx data corrected assuming each wire spends 12.5% of time in tension

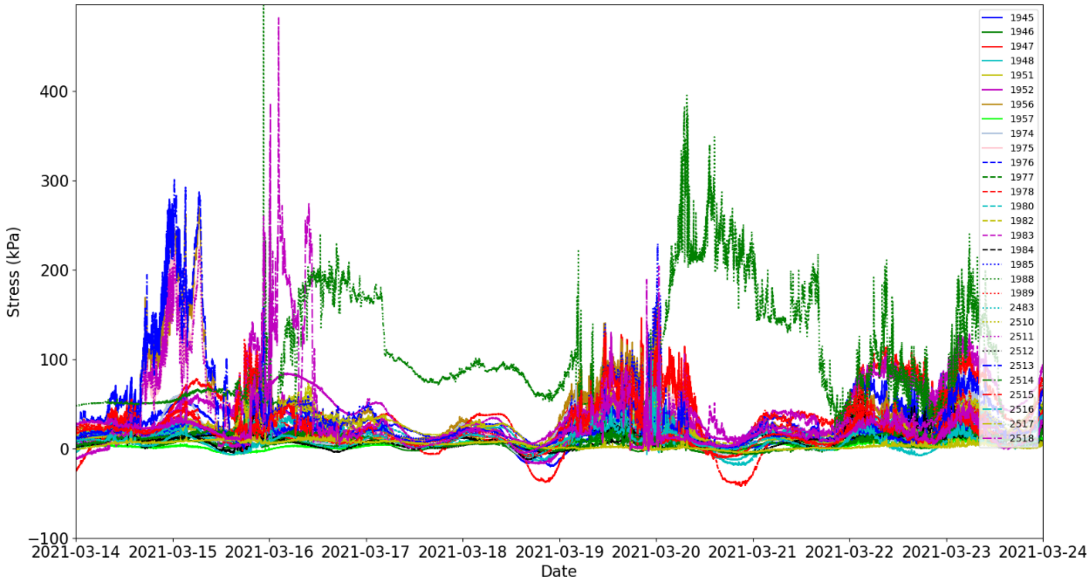

Figure 6. SIDEx data corrected assuming each wire spends 20% of time in tension

A Mohr-Coulomb failure envelope was generated using the VWSG stress measurements. This was done to test whether observed stresses are consistent with the hypothesis that compressive shear faulting operating at low confinement biaxial compression is the dominant failure mode of sea ice, [9]. We follow the same method as Weiss et. al 2007 [3], apart from our data convention setting compressive stress be positive and tensile stress be negative. We plot the failure envelope using 2 different methods. For the first, the primary and principal stress are plotted against each other (p vs. q), and then plotted again inverted (q vs. p) (Figure 7). The upper and lower Coulombic boundaries drawn on the figure are:

$$B_{U1} = \sigma_c + mq \tag{6}$$

$$B_{L1} = \frac{(p - \sigma_c)}{m} \tag{7}$$

Where B_{U1} and B_{L1} denote the upper and lower boundaries, respectively, of the Coulombic failure envelope in principal stress space. Any point outside of these bounds implies mechanical failure of the ice. p is the primary principal stress, q is the secondary principal stress, σ_c is the uniaxial compressive strength of ice, and m is the experimentally determined slope of the low-confinement segment of the failure envelope as calculated by Schulson et. al, 2006 [24]. σ_c was held at 250 kPa as in Weiss et. al, and m was set to be 5.2.

The second method was to plot the pressure (eq, 8) vs. the maximum shear stress (eq. 9) (Figure 8).

$$\sigma_N = \frac{(p+q)}{2} \tag{8}$$

$$\tau \quad = \frac{(p-q)}{2} \tag{9}$$

Here, the Coulombic boundaries are:

$$B_{U2} = \tau_0 - \mu\sigma_N \tag{10}$$

$$B_{L2} = -\tau_0 + \mu\sigma_N \tag{11}$$

Where B_{U2} and B_{L2} denote the upper and lower boundaries, respectively, of the Coulombic failure envelope, under normal stress and shear stress. Here, τ_0 is the cohesion of the material and μ is a friction coefficient. These were set to be 40 kPa and 0.7, respectively, in accordance with Weiss et. al.

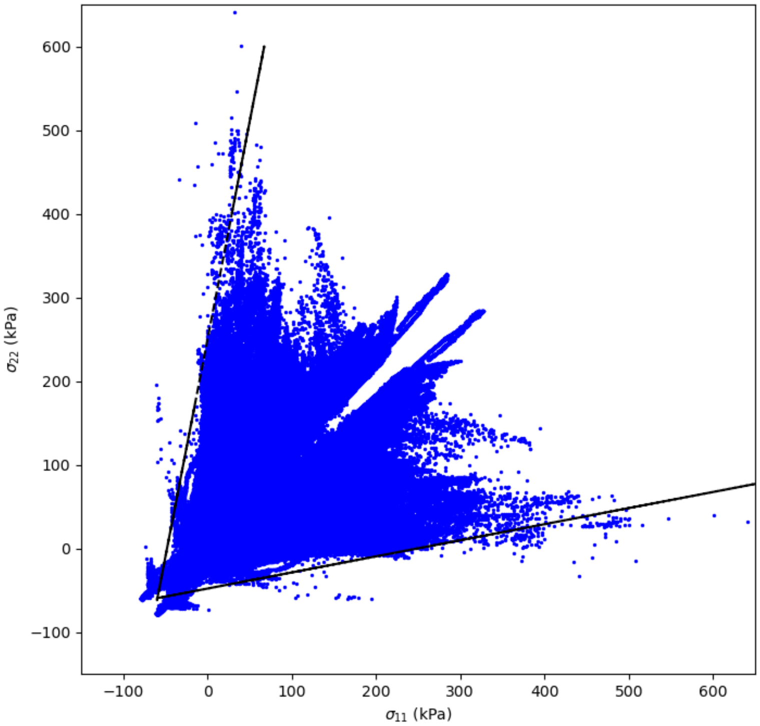

Figure 7 (top). Mohr-Coulombic failure envelope plotted as p vs. q.

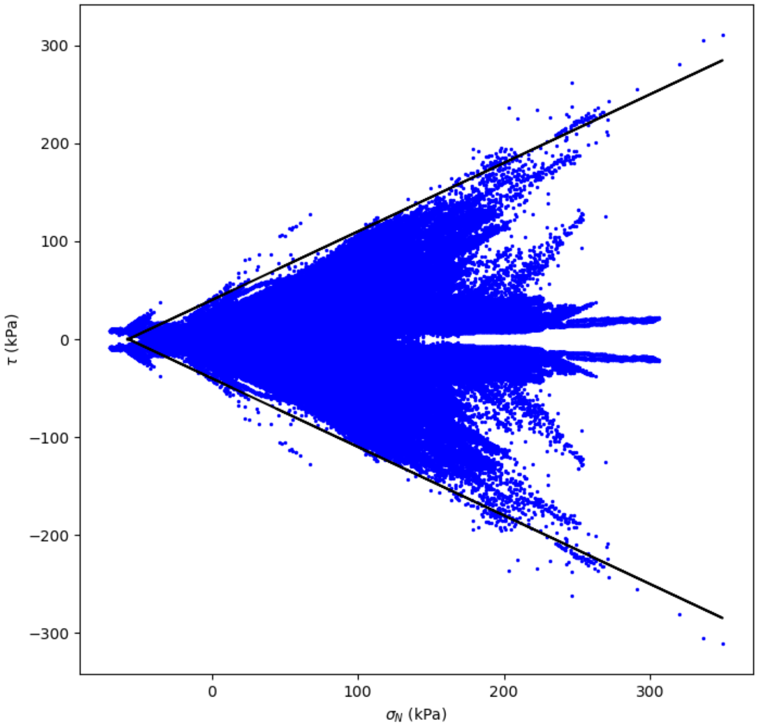

Figure 8 (bottom). Mohr-Coulombic failure envelope plotted as σ_N *vs.* τ.

3.3 Strain Measurements

Sensors of multiple types were deployed at SIDEx to characterize strain. These sensors had varying spatial and temporal resolutions and provide unique accounts of pre-fracture and post-fracture deformation. Strain measurements were obtained by two Leica Nova TM50 high precision automated total stations [25], a GAMMA Portable Radar Interferometer II (GPRI) [26], and 12 SATICE GNSS Buoys [27]. The Leica TM50 along with an array of retroreflectors installed on steel posts provided laser strain observations and is commonly referred to as the Laser Strain Observing system (LSO). The LSO measures sub-mm scale deformation on prismatic reflectors spaced in an array around a central scanner. 2 LSO stations were deployed, one at the Main Camp and the other at the SIDEx backup tent area, hereafter referred to as East Camp, with 64 reflectors spread throughout a roughly 6km^2 area. Some reflectors were targeted by both scanners so that results are collocated and merged into a single dataset. The GPRI is another instrument capable of measuring small-scale deformation, as it can resolve shifts on the order of 0.1mm at 1 km [26]. The GPRI is a Ku-band (17.2 GHz, 1.74cm wavelength) radar that scans and measures backscatter from geographical features within a set radius. These scans are analyzed to determine phase changes in backscatter from one time to the next over a roughly 5-minute cycle. The observation radius was initially 8.4km from March 5th to March 14th but was adjusted to 4.2km on March 14th at 19:20 UTC. 12 geodetic-quality GNSS buoys offered a larger-scale view of deformation with the best temporal resolution available. These buoys recorded one GPS measurement per second and provide valuable information during the periods when the LSO and GPRI are scanning.

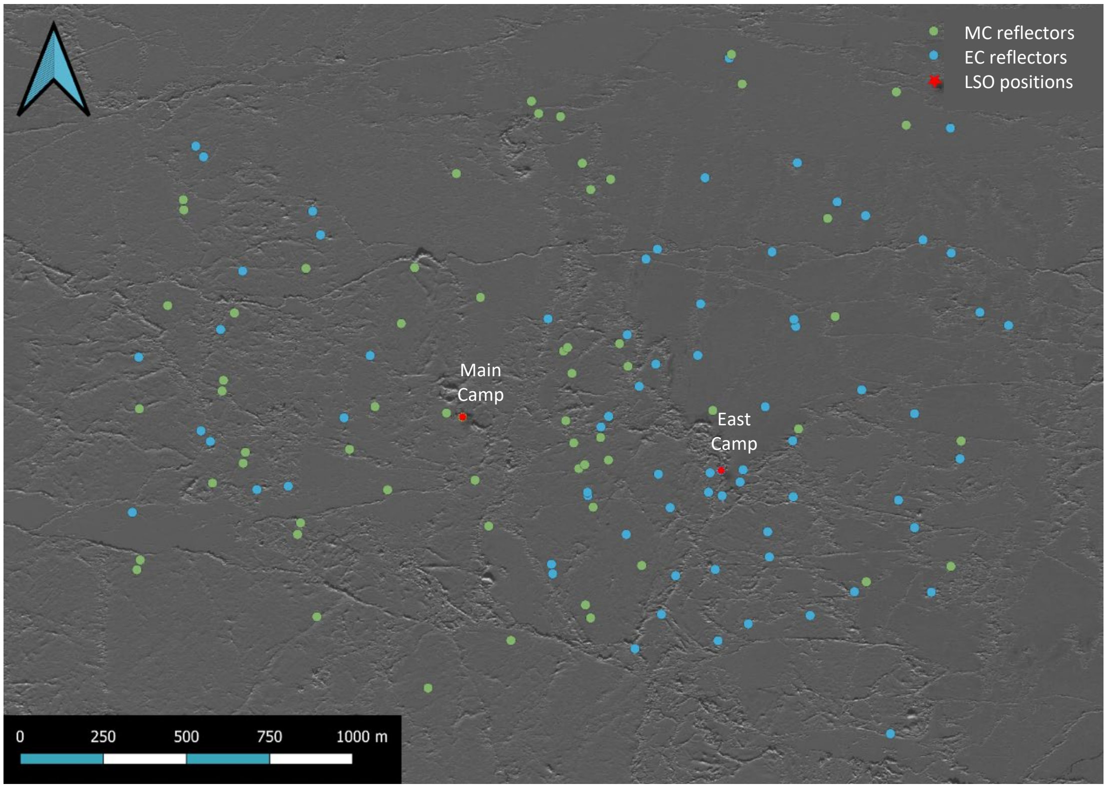

Figure 8. Map of the LSO reflectors with the Main Camp (MC) and East Camp (EC) LSO scanners marked in red.

3.4 Satellite Imagery

The three primary satellite imagery sources used in this report are Maxar-Digital Globe Worldview (WV), RADARSAT Constellation Mission (RCM), and COSMO-SkyMed imagery. WV imagery constitutes the baselayer of most LSO and VWSG plots showing the spatial distribution of data. RCM is comprised of 3 satellites that used C-band SAR (5.405 GHz) to capture large scale images with a resolution between 3 and

100m depending on the mode used. RCM is used to analyze ice motion at the multi-floe scale, providing insight into the floe-floe interactions between the Camp, East, North, and West Floes, along with their respective sub-floes. TerraSAR-X and COSMO-SkyMed satellites were used to obtain high spatial resolution images multiple times per day. The TerraSAR-X satellite provided a stripmap mode SAR over camp, generating twice daily images at 3m resolution. COSMO-SkyMed provided twice daily spotlight mode imagery at a 1m resolution. Stripmap mode provides an uninterrupted image over a fixed swath of terrain as the antenna maintains a fixed angle and position over its track. Here some of the smaller cracks cannot be observed, but the geographical context is much better preserved. Spotlight mode provides a higher resolution view of a specific area as the antenna changes angle to increase the effective synthetic aperture length, while sacrificing the overall image size, and precluding continuous imaging along a track. Stripmap was more likely to capture the camp location and context around it reliably. Spotlight mode provided better detail, but with high risk of missing the camp altogether if drift forecasts were incorrect, resulting in tasking the wrong area. Each mode is used in tandem with the others to best explain SIDEx fracture events. SAR images were combined in this report with GPRI annotated fractures and VWSG stress data to provide visualizations of ice stress-strain during fracture.

4. Results

4.1. Temporal Variability of Stress

The SIDEx data shows high temporal variability. Periods of elevated, highly variable stress commonly lasted several days. As Richter Menge et al. found for similar periods of high frequency activity, these periods are likely primarily driven by ice dynamics. The dynamically active periods (DP) are separated by low activity periods (LP), during which smaller, smoother, and often diurnally cycling stress signals are observed. The smooth signal is likely associated with only thermal expansion or contraction stress. DPs generally occurred around times when SIDEx strain sensors detected a fracture on or near the floe. We identify a DP as a range of time where two or more 'stress events' occurred within 30 minutes of each other, without a 30-minute calm period on either side. 'Stress events' occur when any sensor experienced a stress change of 15 kPa in one minute. DP status was calculated for each minute between 14 March and 24 March. The average duration of a DP was 1.73 +/- 2.56 hours, with a maximum of 9.45 hours. LPs lasted an average 3.20 +/- 9.11 hours, with a maximum of 59.48 hours.

Three periods that included known fractures around stress DPs are analyzed in this paper. These are:

1. 14:30 – 17:30 UTC, 14 March 2021
2. 12:00 UTC, 15 March 2021 – 01:00 UTC, 16 March 2021:
3. 01:30 UTC, 19 March 2021 – 06:00 UTC, 20 March 2021:

These will henceforth be referred to as Fracture Period 1 (FP 1), Fracture Period 2 (FP 2), and Fracture Period 3 (FP 3). The temporal heterogeneity of stress can be seen through the variability of stress events that occur in each period. For each stress event, a power index (PI) accounting for both the number of sensors surpassing the +/- 15 kPa threshold and the total magnitude of stress change was calculated according to (eq. 12).

$$PI = \sum_i^n \frac{(d\sigma_i)^{1.5}}{100} \tag{12}$$

Here n is the total number of sensors that recorded a >15 kPa change and $d\sigma_i$ is the stress change of the ith sensor within that group. During FP1 there were 19 stress events. An average of 3.00 ± 1.11 sensors crossed the event threshold with an average PI of 5.90 ± 6.93. The maximum PI for FP1 was 32.02. There were 148 stress events for FP2, with an average sensor count of 2.03 ± 1.53 and an average PI of 5.38 ± 9.56. The maximum PI for FP2 was 68.30. FP3 saw 327 stress events, with an average sensor count of 3.04 ± 3.45 and an average PI of 4.67 ± 8.13. The maximum PI of FP3 was 81.32.

The degree of correlation between consecutive measurements in our stress record is important to understanding which process dominates the overall signal. Thermal stresses tend to be well correlated because they typically consist of a smooth diurnal signal (Figure 13). Dynamic stresses tend to have sharp temporal deviations and exhibit lower correlation (Figure 12). Temporal autocorrelation analysis was used to determine the predictive power one measurement has over consecutive measurements (eq. 13). Across the 10-day record we find the signal correlated to 0.92 after 3 hours, 0.87 after 6 hours, 0.80 after 9 hours, and 0.76 after 12 hours.

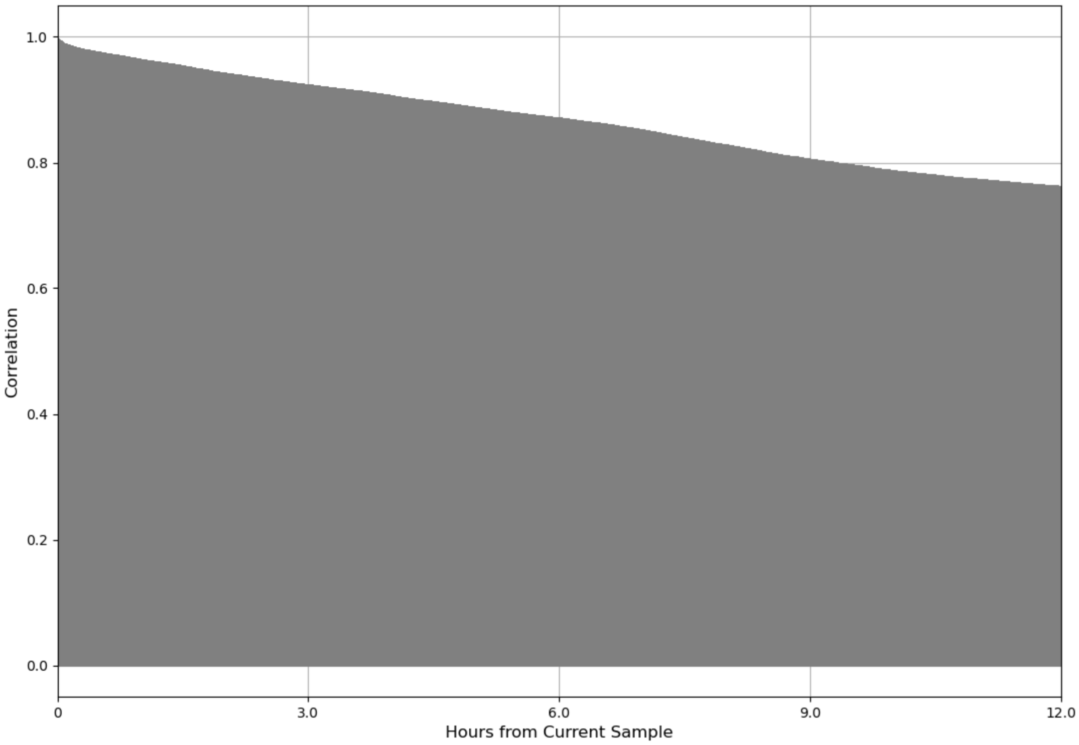

Figure 10. Temporal autocorrelation from 14 March to 24 March.

Over periods which included DPs and LPs, the overall correlation maintains a higher correlation like that of a LP. Such a trend can be seen in a 3-day period from 12:00, 15 March to 12:00, 18 March, which included both FP 2 and the proceeding low-dynamic activity period (Table 2). While the 3-day correlation maintains a similar value to the correlation during the LP, the correlation during FP 2 dips sharply. This is due to the higher prevalence of high-frequency events over that period. Since the 10-day period maintains a correlation similar to that of a period with minimal dynamic activity, we believe thermal stresses dominate the overall stress signal from 14 March to 24 March.

	3-hour	6-hour	9-hour	12-hour
10-day period (03/14 – 03/24)	0.92	0.87	0.80	0.76
3-day case study (12:00 03/15 – 12:00 03/18)	0.92	0.88	0.82	0.78
Fracture Period 2 (12:00 03/15 – 01:00 03/16)	0.73	0.61	0.58	0.53
Intra-FP2 LP segment (06:00 03/17 – 12:00 03/18)	0.95	0.89	0.84	0.79

Table 2. Temporal autocorrelation values for 10-day duration, with a case-study of a 3-day period from 12:00, 15 March to 12:00, 18 March.

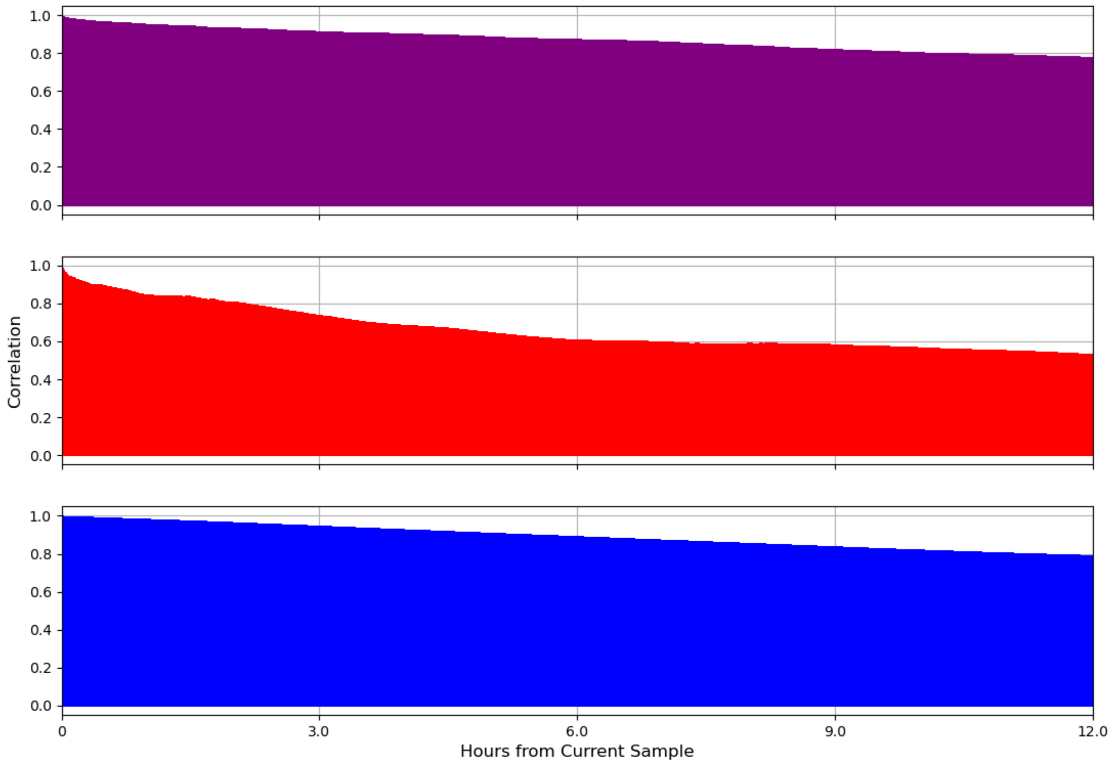

Figure 11 (top). Temporal autocorrelation from 12:00, 15 March to 12:00, 18 March

Figure 12 (middle). Temporal autocorrelation during FP 2

Figure 13 (bottom). Temporal autocorrelation during Inter-FP2, from 06:00, 17 March to 12:00, 18 March

4.2. Spatial Correlation

A spatial correlation analysis was used to assess the degree of spatial coherence in the primary principal stress magnitude and test the influence of floe integrity and ice thickness on stress coherence. Pairwise correlation coefficients were calculated between each VWSG pair and then for each VWSG and the average stress from 14 March to 24 March. The average correlation between sensors was 0.408 with a standard deviation of 0.258 (Table 3). The maximum correlation was 0.958 and the minimum was -0.316. Unsurprisingly, we find that the degree of correlation was affected by the ice integrity between pair members. Sensors on the Camp North floe (1956, 1975, 2511, and 2513), for example, were separated from the sensors on the Camp East, Central, and West (Camp ECW) floes by an WNW-ESE fault located ~1km to the North of camp after 14 March. The 10-day average correlation between North Floe sensors was 0.933 (Table 4), and the correlation between Camp ECW sensors was 0.435. The correlation between sensors on Camp North with the sensors on Camp ECW was only 0.293. The lower correlation on Camp ECW compared to Camp North is likely due to the difference in fracture activity within the two floes. Camp ECW experienced many fractures over this period, whereas Camp North experienced no fractures through the sensor array until 19 March, none of which separated the sensors on this floe (Figure 2). The low correlation between the sensors on the two floes is expected; the fracture separated the two for almost the entire experiment duration.

Type	Avg. Correlation	Standard Deviation	Maximum	Minimum
Sensor to Sensor	0.408	0.258	0.958	-0.316
Sensor to Stress Average	0.635	0.179	0.842	-0.848

Table 3. Correlation coefficients between sensors and between each sensor and the stress average.

Location	Sensor Quantity	Sensor-Sensor Corr.	Corr. w/ Average Stress	Corr. w/ Camp sensors	Corr. w/ North sensors
Camp ECW	26	0.416	0.626	0.435	0.293
Camp North	4	0.379	0.694	0.933	0.293

Table 4. Average correlation coefficients for sensors on Camp ECW and Camp North.

The correlation between sensors on Camp ECW also changes with respect to time as the floe breaks up. During DP 1 Camp ECW was a contiguous floe. The sensors on it had an average correlation of 0.675, compared to 0.309 during DP 2 and 0.334 during DP 3, when fractures had broken up Camp ECW. We also see inverse correlations between sensors on adjacent floes during some events. This is consistent with fracture relieving stress on one floe while transferring it to another; we hypothesized that we would see this behavior of changing floe geometry and contact adjusting stress pathways through the ice. This can be seen both during DP 1 and over the full 10-day period between V1988 and the other sensors. For DP 1, sensors on Camp North had an average correlation with each other of 0.982 and an average correlation with Camp ECW sensors of -0.571. We hypothesize that this occurred because the far field stress that was transmitted through the ice moved through a chain of contacts that included Camp North but not Camp ECW. While Camp North experienced primarily dynamic stresses during this time, Camp ECW experienced primarily thermal stresses, appearing to be temporarily uninvolved in far field stress transfer. The stress at sensor 1988 had an average correlation with all other sensors of -0.152 over the 10-day period with a maximum of 0.076 and a minimum of -0.316. This unique behavior appears to be due to contact geometry. 1988 was located at a contact point between the Camp Central 1 and Camp Central 6, on an asperity that also extended below Camp Central 5 and above Camp Central 7.

We find that the average correlation of each site to the average stress (0.635 +/- 0.179) is stronger than the correlation between sensors. This is similar to the correlation found by *Richter Menge et. al* [18] (0.65 +/- 0.14) during the SHEBA field experiment and supports their hypothesis that the average stress is a better representation of regional stress than any individual sensor. The high degree of variation between our sensor observations and the spatial correlation of those on the same floe, however, suggests that determining a representative regional stress may require sampling on multiple floes over a larger area than this, or other prior studies, have executed.

Camp ECW, which exhibited lower stress correlation even prior to fracture, had higher thickness variability. Because of this, we tested the relation between average stress and ice thickness at each site (Figure 14). The correlation was found to not be statistically significant with a p-value of 0.103.

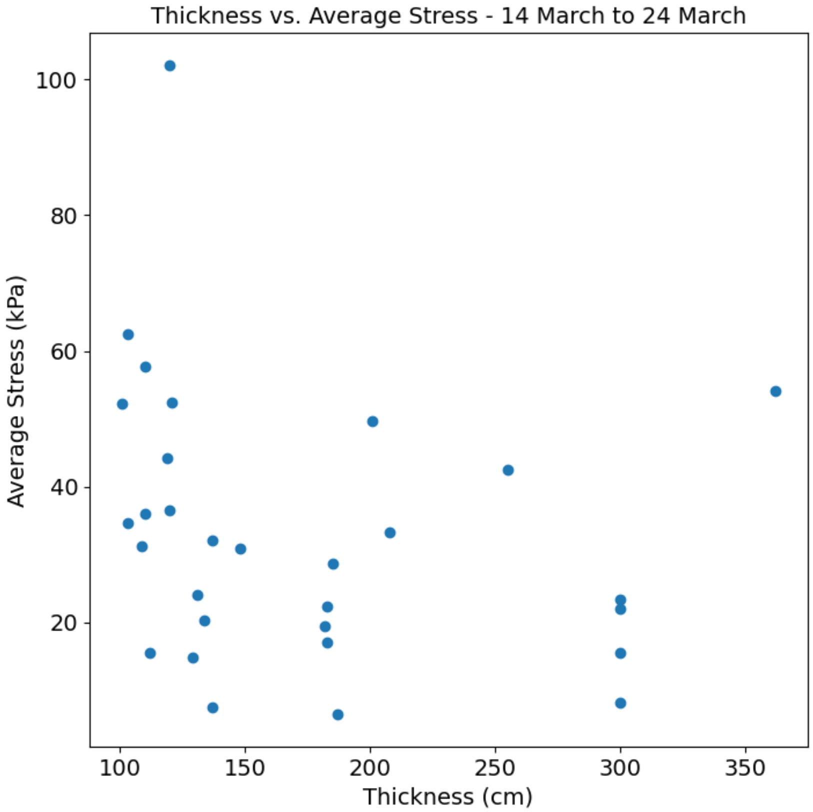

Figure 14. Correlation between the ice thickness and average stress at each site.

4.3. Fracture Period Analysis

4.3.1. Pre-Fracture Period History

Prior to the events we observed and discuss below, the ice floe had undergone considerable prior deformation. Immediately preceding the experiment, however, the ice had an opportunity to bond back into a contiguous, if flawed, sheet. During the 9-day period from 22 February to 3 March ice motion in the Beaufort Sea all but ceased in this area under cold, nearly windless conditions. There were no open leads and few recently fractured leads visible in the ~100km scale region during our scouting missions to locate a suitable floe for the experiment (28 February - 4 March). GPS data from our floe indicated that ice motion resumed on 4 March, beginning a westward drift that continued until 9 March. During this time fast ice detached from shore along the entire southern and eastern Beaufort coastline all the way from Point Barrow to to Banks Island. This motion caused many parallel large scale leads/shear lines, here referred to collectively as Linear Kinematic Features (LKF), to form between 3 March and 5 March. These were oriented from SSW to NNE, and individual members of the LKF set were situated several km both east and west of the camp. Southward drift followed from 10 March to 12 March compacting the ice against the coast. At this time the East and West Floes were separated by leads on either side of the Camp Floe (Figure 15). On 13 March westerlies resumed, continuing through the start of the first observed fracture period, when fractures began passing through the camp floe.

4.3.2. Fracture Period 1: 14:30 – 17:30, 14 March

Fracture Period 1 (FP 1) consists of a dynamic period during which a fracture starts WNW of camp and propagates ESE across the Camp + Camp North Floe, separating the two (see Figure 2 in Methods section for floe naming). The fracture occurred during a period of larger scale motion in the Beaufort Sea, which exerted shear in the floe area. The stress observations, together with remote sensing imagery, appear to indicate that large scale shear brought the Camp + Camp North Floe into contact with its neighbors at a small portion of its perimeter. This local contact concentrated far field stress across only a portion the floe, resulting in fracture and subsequent deformation.

RadarSAT and Cosmo SkyMed imagery show the context of the floe and its neighbors. The ice west of camp moves NE between 13 March (Figure 15) and 16 March (Figure 16), resulting in a right lateral shearing along the western LKF. Meanwhile, the

LKF east of the camp also exhibits right lateral shear as ice to the east moves south, closing a previously open lead. Total shear over the three da period on the western LKF is approximately 3km, while total shear on the eastern LKF is approximately 1km.

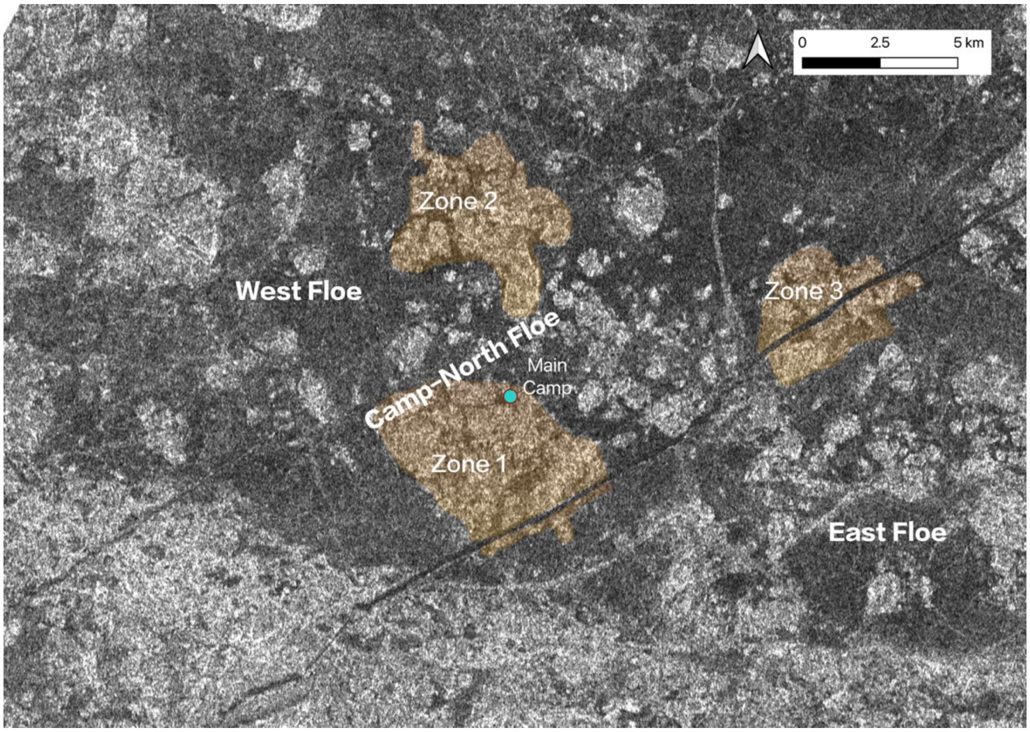

Figure 15 (top). RadarSAT image taken on 15:50, 13 March with features highlighted. Motion arrows indicate motion relative to the camp center point, the entire field of view is also moving WNW. Shear can be seen by relative displacement of components of the three zones.

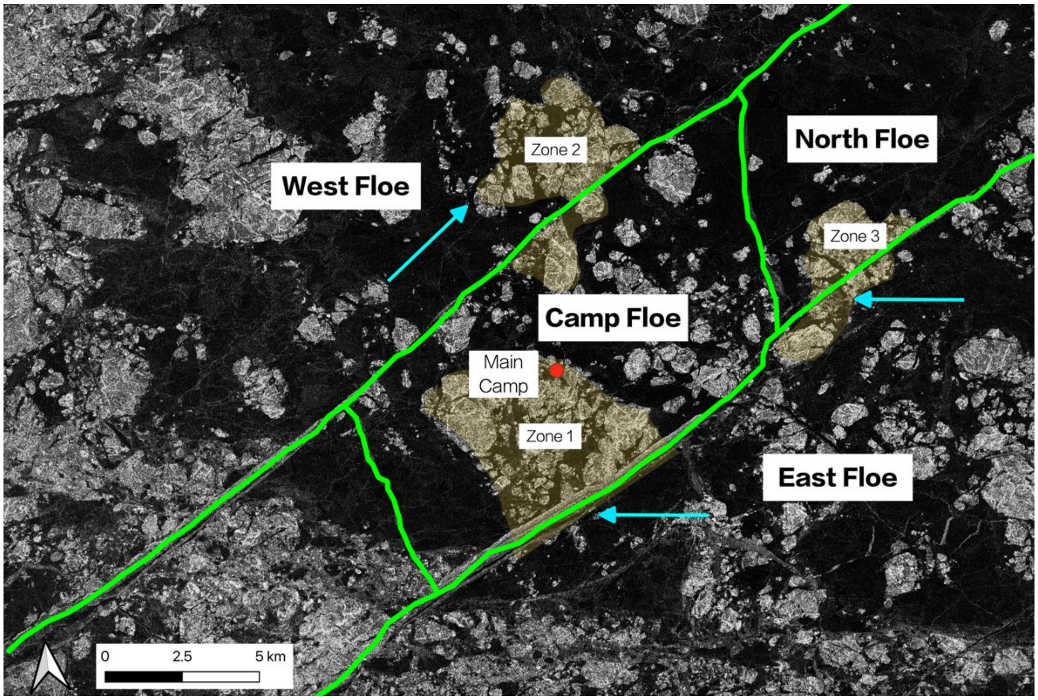

Figure 16 (bottom). Cosmo-SkyMed image taken on 14:49, 14 March. Ice movement is noted by blue arrows. The green lines denote leads.

The sides of the lead come into compressive contact on 13 March along a section about 2km in length approximately 6.5 km to the east of camp, and ridge building was noted at this location during reconnaissance flights (Figures 15, 19). The closure of the west LKF also occurs sometime late on 13 March or early on 14 March to the NNW of camp. Compression between these points, coupled with ongoing shear appears to be the cause of a fracture forming from just south of the west contact point to the east contact point; a zone we would expect to be experiencing tensile stress.

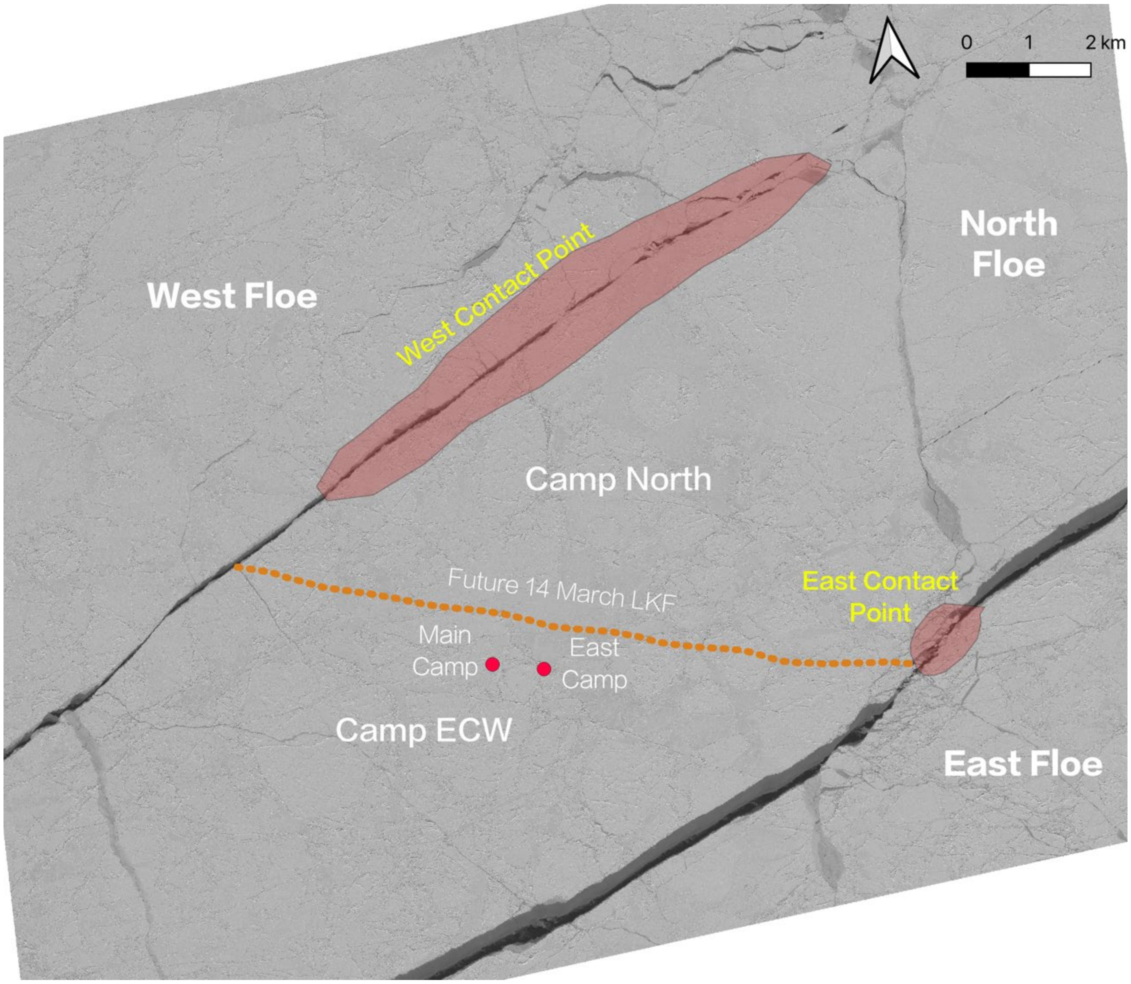

Figure 17 (top). Regional context around the Camp Floe at 22:38, 13 March.

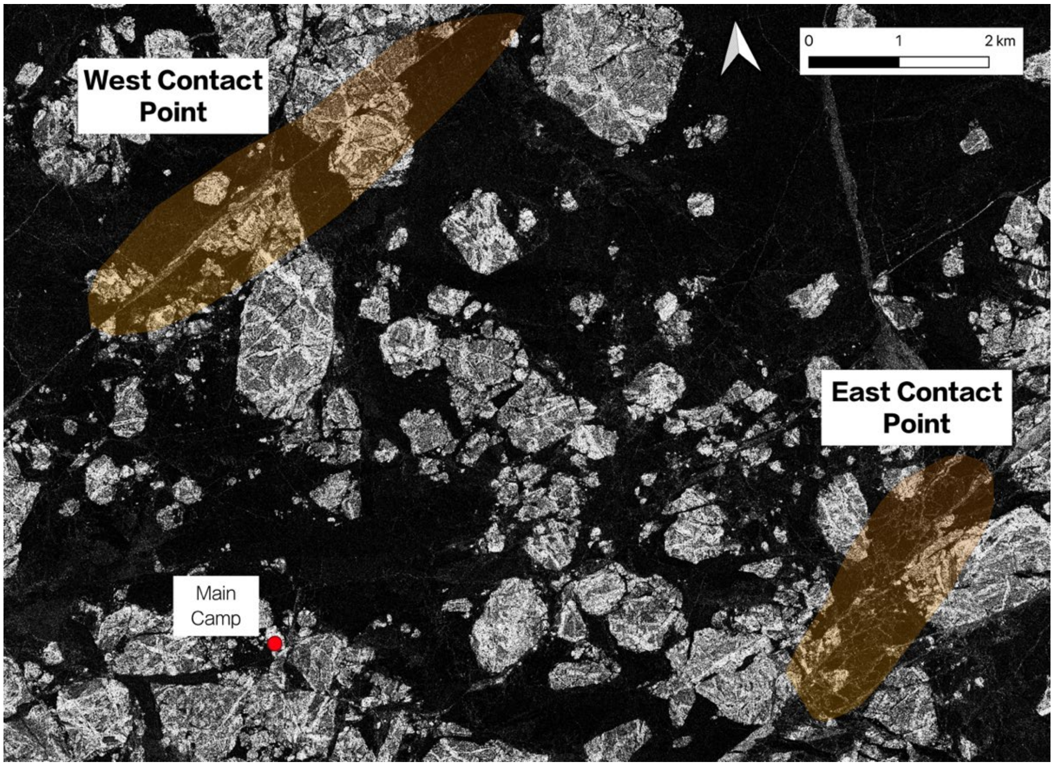

Figure 18 (middle). East and west contact points at 14:49, 14 March.

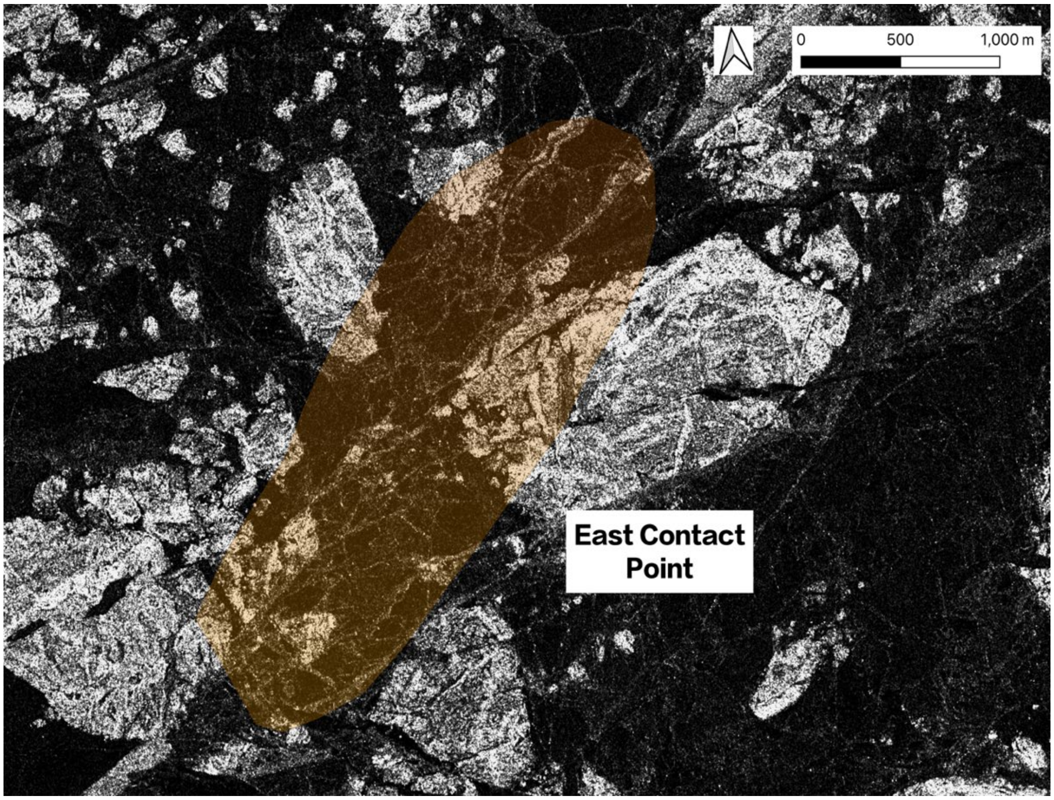

Figure 19 (bottom). East contact point at 14:49, 14 March

This hypothesized mode of fracture, and propagation from a high tensile stress area in the west toward the east is supported by the morphology of the crack; it was observed to open more widely to the west. GPS buoys indicate a clockwise rotation of the North Floe occurred post-fracture (relative to Camp Floe) with the crack widening to the west (Figure 20). The fracture initiation and propagation were also further captured by the GPRI. An interferogram calculated between 15:15 and 15:30, 14 March first shows a discontinuity in the fringe pattern associated with a fracture entering the field of view from the west (Figure 21). The discontinuity then propagated WNW-ESE through the array sometime during the interferogram calculated 15:30 and 16:00, 14 March (Figure 22).

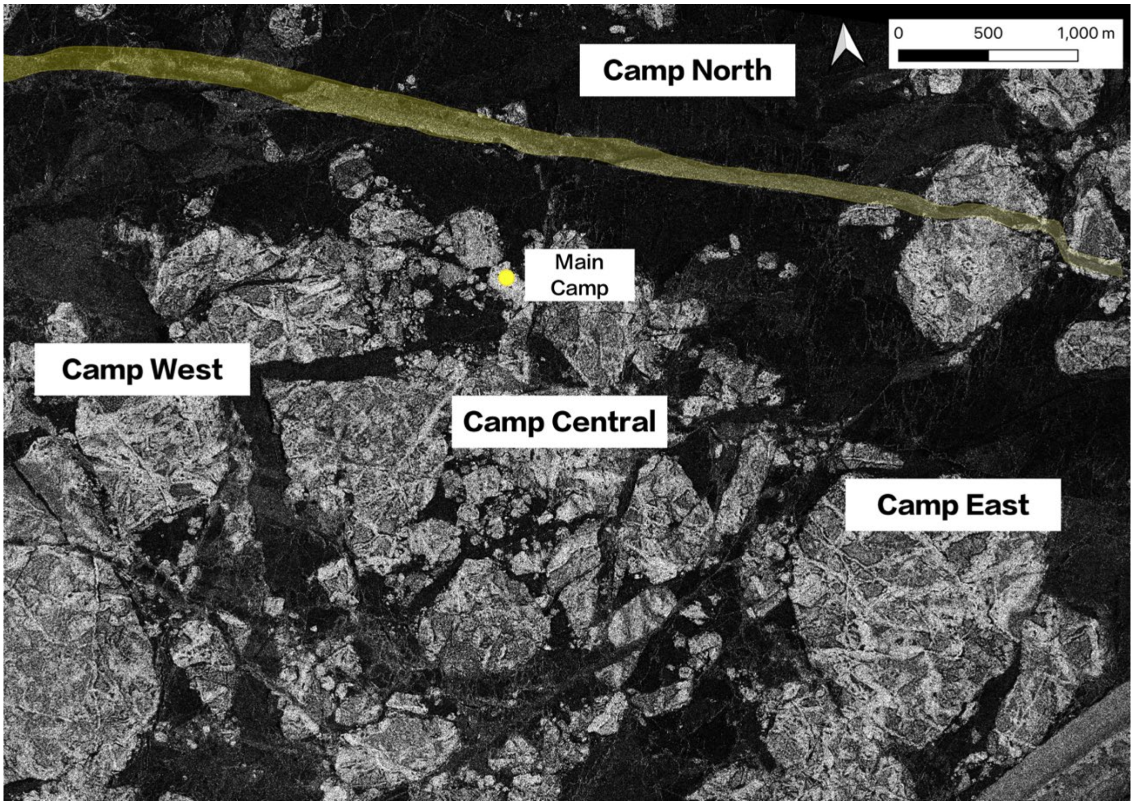

Figure 20. Crack displacement visualized in Cosmo-SkyMed SAR imagery on 04:21, 15 March.

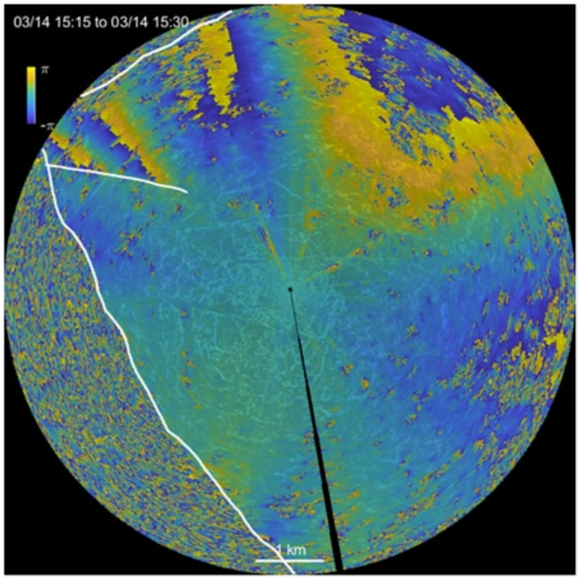

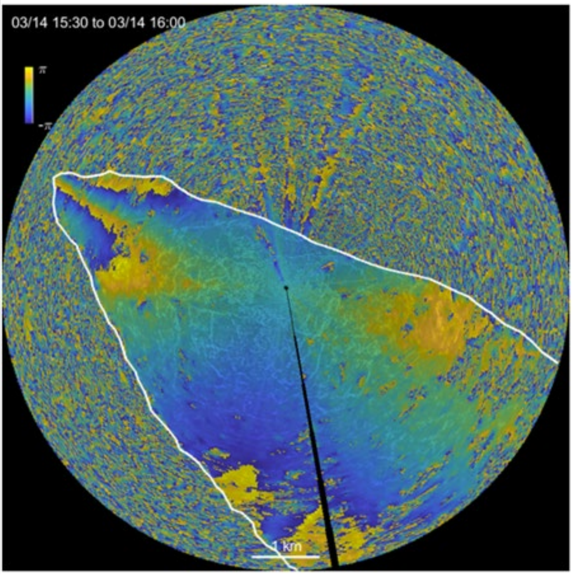

Figure 21 (left). GPRI interferograms calculated between 15:15 and 15:30.

Figure 22 (right). GPRI interferograms calculated between 15:30 and 16:00

We are interested in examining the stress state in the ice at the time of this failure. Based on our understanding of the geometry of the event, sensors to the north of the crack were in a stress transfer pathway between the two contact points that were in compressive shear. We see relatively little stress in the Camp ECF or Camp North Floes, and very little change in stress (<10kPa) during the time that the fracture first began propagating in the GPRI data; however, this early fracture propagation was well outside the stress observing array. Beginning on 15:58, 14 March we see an abrupt change in stress state within our sensing array. Sensors to the north of the fracture on Camp North experience large increases in compressive stress, and those south of the fracture on Camp ECF experience a modest decrease in compressive stress. Stress increased observed at sensors 1956, 1975, 2511, and 2513 in Camp North were oriented at a 16° incline to the crack (Figure 23).

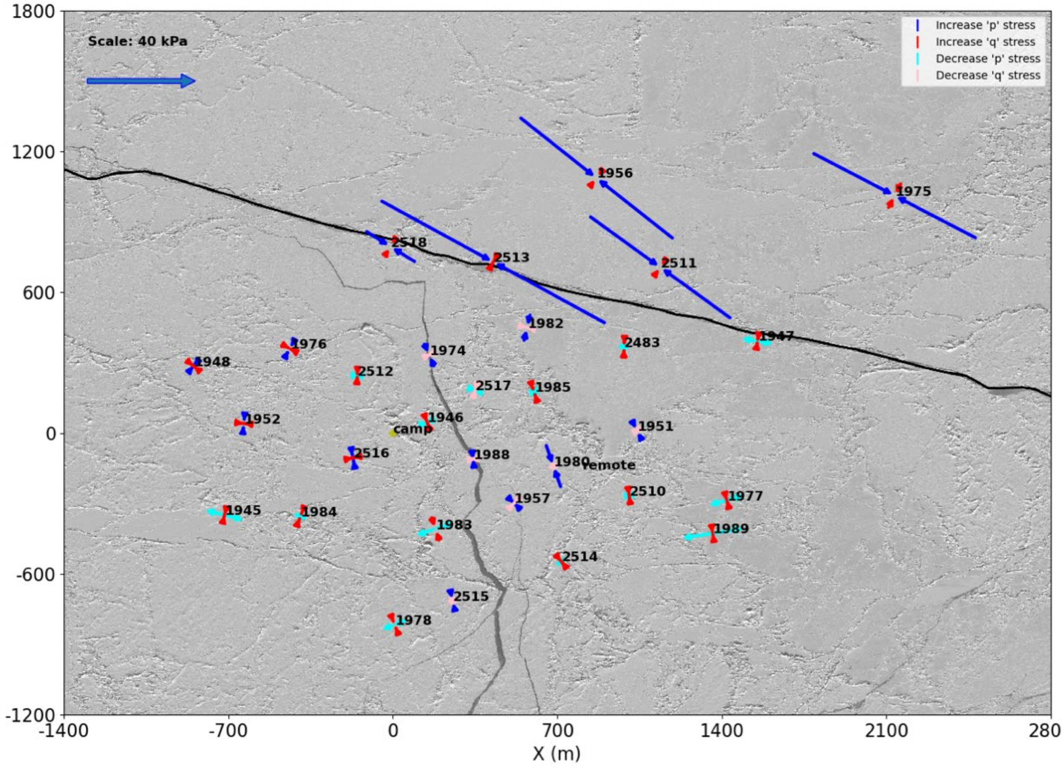

Figure 23. Stress change from 15:58 to 15:59, 14 March.

To assess if this incline is reasonable, we transformed the stress into a coordinate system parallel to the crack, using planar stress transformation equations.

$$\sigma_{||} = \frac{p+q}{2} + \frac{p-q}{2}cos2\theta + \tau_{xy}sin2\theta \tag{13}$$

$$\sigma_{\perp} = \frac{p+q}{2} - \frac{p-q}{2}cos2\theta - \tau_{xy}sin2\theta \tag{14}$$

$$\tau_{x'y'} = -\frac{p-q}{2}sin2\theta + \tau_{xy}cos2\theta \tag{15}$$

Where $\sigma_{||}$ is the normal stress parallel to the crack, $\sigma_{\perp}$ is the normal stress perpendicular to the crack, and $\tau_{x'y'}$ is the shear stress along the ice boundary. θ is considered positive counterclockwise relative to the original p-stress orientation. Averaging the Camp North sensors together, p was 78 kPa, q was 29 kPa, and θ was 16°. This yields a $\sigma_{||}$ of 75 kPa and a $\tau_{x'y'}$ of 13 kPa. Since both the west and east LKF were experiencing right lateral shear, this stress state is reasonable and agrees with regional-scale ice movement.

The stress orientation in the Camp North Floe remained constant for the duration of FP 1, indicating that the WNW-ESE compressive shear persisted between the contact points. While the Camp North Floe experienced large and variable dynamic stresses from 15:58 to 17:30 (the duration of FP 1), the Camp Floe experienced very little stress. The Camp Floe was not in contact with the either the West or East Floe at this time, resulting in the Camp North Floe taking the full load. Concentration of stress between geometric contact points is clearly loading the ice heterogeneously, resulting in a deviation from continuum behavior at this scale.

The stress signal from the North Floe sensors indicate that hardening was occurring at one or both contact points while undergoing compressive shear. The signal displays a quickly fluctuating stress superimposed over an increasing stress (Figure 24), angled slightly to the crack. The period is highly active; 18 stress events occurred during this time compared to only 3 events in the 16 prior hours. This indicates that ice was failing at the contact points since no other fractures were seen in this pathway, likely due the contact geometry between floes. As the ice continued to rotate, narrow regions of the floe were in contact with other bodies (Figures 18, 19). We speculate that this caused the ice in contact with the loading body to fail, resulting in a partial unloading of stress throughout the floe. The average stress magnitude also increased, indicating the pack was strengthening (the weaker ice was being removed, leaving behind stronger ice). Stress in the North Floe increased from an average 44 +/- 4 kPa to 108 +/- 13 kPa over the 92 minutes, reaching a peak stress of 182 kPa at 17:15. This coincided with a 1.8° clockwise rotation of the North Floe, calculated from GPS buoys. We speculate that as one layer of ice failed, the continued rotation caused the next layer of ice to have a broader contact geometry. As the contact geometry broadened, stress was distributed over a larger area, permitting a larger overall load to be seen throughout the North Floe. This pattern continued from the fracture propagation through the end of FP 1.

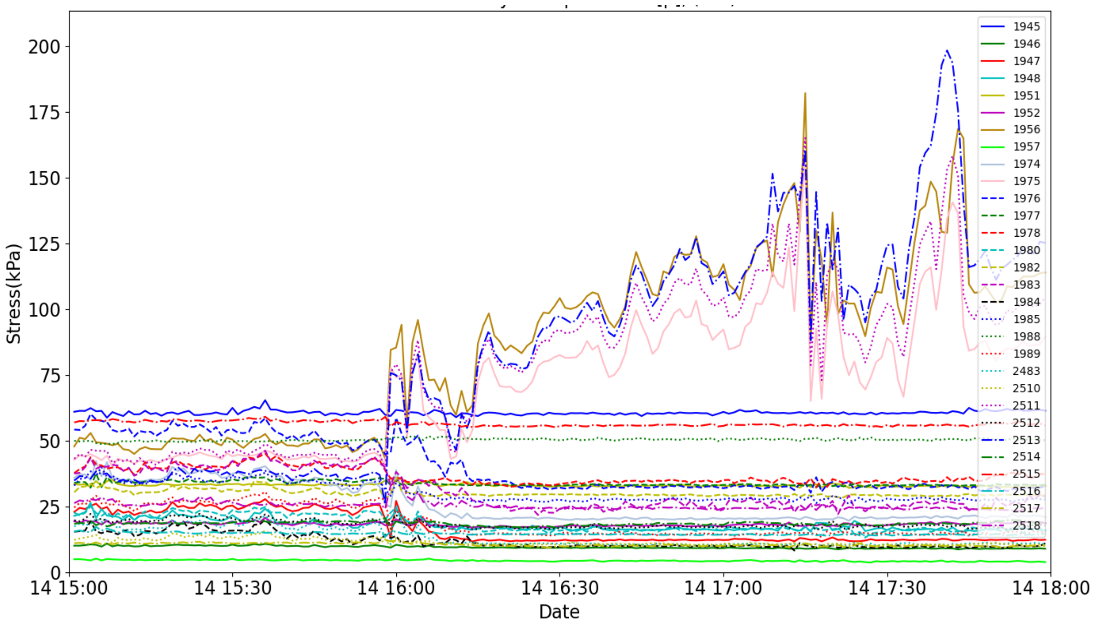

Figure 24. Stress vs. time during FP 1.

4.3.3. Inter-FP 1: 17:30, 14 March to 12:00, 15 March

The time between Fracture Periods, referred to as Inter-FPs, are discussed to provide context to each period, although no fractures occurred within the sensor array during either Inter-FP 1 or Inter-FP 2. The behavior of Inter-FP 1 is largely similar to the final hour of FP 1. Stress events continued to occur in the North Floe until around 09:00, 15 March. This intermittent period was omitted from the FP 1 because no new fractures were observed in the local area. Instead, Camp North continued to experience high-frequency stress events from the progressive failure at the west and east contact points between Camp North and the East Floe and West Floe. The lead separating the Camp Floe from the North Floe does not close until the beginning of FP 2, meaning no floe-floe interaction occurred between these floes within the array. The Camp Floe sensors record primarily thermal stress for the duration of this period, and do not observe stress events until FP 2 begins.

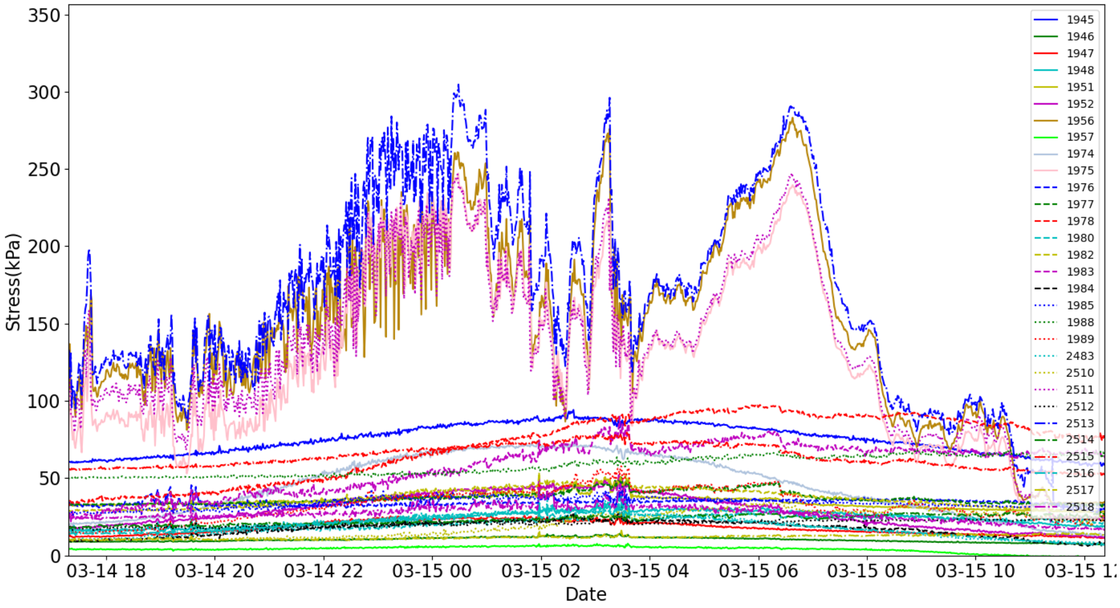

Figure 25. Stress vs. time during Inter-FP 1.

4.3.4. Fracture Period 2: 12:00, 15 March to 01:00. 16 March

Fracture Period 2 (FP 2) occurs around a time when extensive breakup and shear had occurred throughout Camp South and Camp West floes. The ice had resumed a westward drift and there was little differential movement of the West and East Floes relative to the Camp Floe. During this time a fracture propagated S-N through the sensor array, separating Main Camp from the Camp East and the Camp West and Camp Central floes from Camp East. Camp Central was broken into 5 smaller floes at this time. Sensors 1976, 1988, and 2518 were located near asperities along the fracture and recorded high-frequency, high-magnitude stresses as the Camp Central floes collided with each other and Camp East. Stress pathways in this environment are seen to be localized and can change rapidly, alternating high loads at different asperities on the order of minutes.

The Cosmo-SkyMed image taken on 14:49, 14 March (Figure 16) shows a regional context similar to 21:46, 16 March. Features on each floe appear to be in the same position, indicating large-scale sliding had stopped near the start of FP 1.

Many new cracks propagated through the Camp Floe from the end of FP 1 to the end of FP 2. Most of these cracks were kilometers from the sensing array, with the largest cracks propagating N-S from the south tip of Camp South, through Camp West, and into the West Floe (Figure 26). Camp Central and Camp East saw cracks propagate NE from Camp South and NW from the East Floe-Camp East contact zone. Evidence of shear can be seen throughout Camp East. This period precedes a majority of Camp East being sheared off the Camp Floe during FP 3, resulting from a continued left lateral shearing along the Camp East-East Floe boundary.

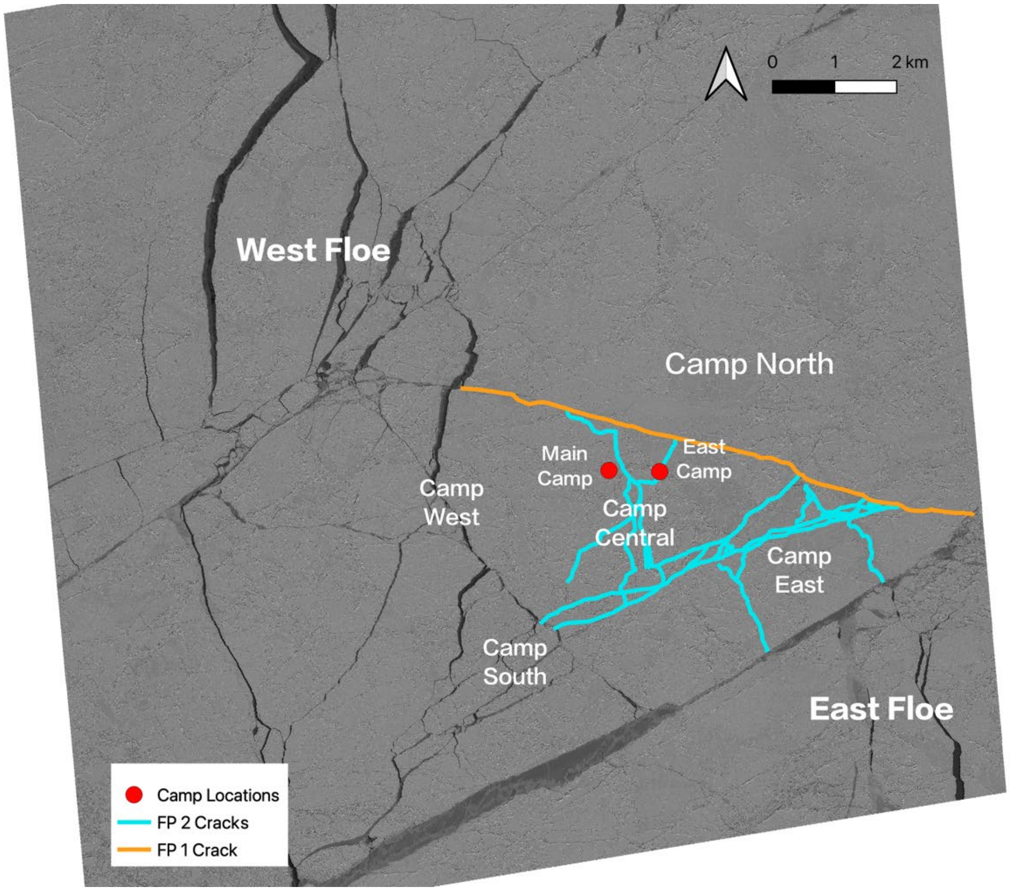

Figure 26. Crack positions in the Camp Central and Camp East floes from a 21:47, 16 March WV image.

During FP 2 multiple fractures propagated through the stress array. The GPRI records the first crack propagation between 16:52 and 17:04, while the LSO records cm-scale displacement at reflectors on or near Camp East, Camp Central 7, 8, and 9.

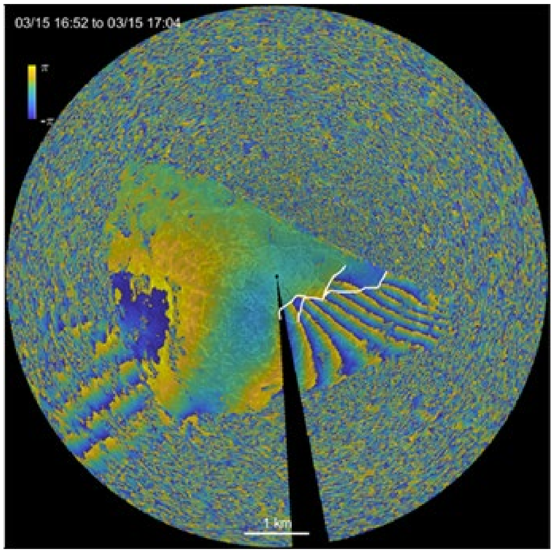

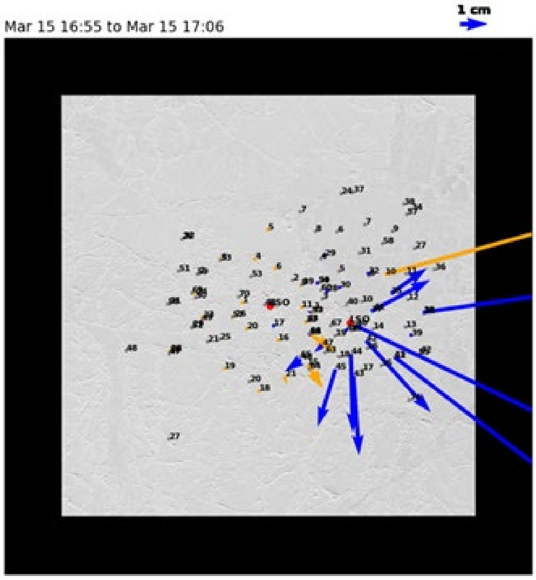

Figure 27 (left). GRPI interferogram calculated from 16:52 to 17:04, 15 March.

Figure 28 (right). LSO reflector movement from 16:55 to 17:06, 15 March.

Little dynamic stress change occurred at the time when the GPRI and LSO observed the fracture. There were multiple stress events preceding the crack propagation. The VWSG array records a decrease in stress in Camp East and Camp Central 1 at 16:45 and continues decreasing until 17:11, including a sharp decrease at 16:49.

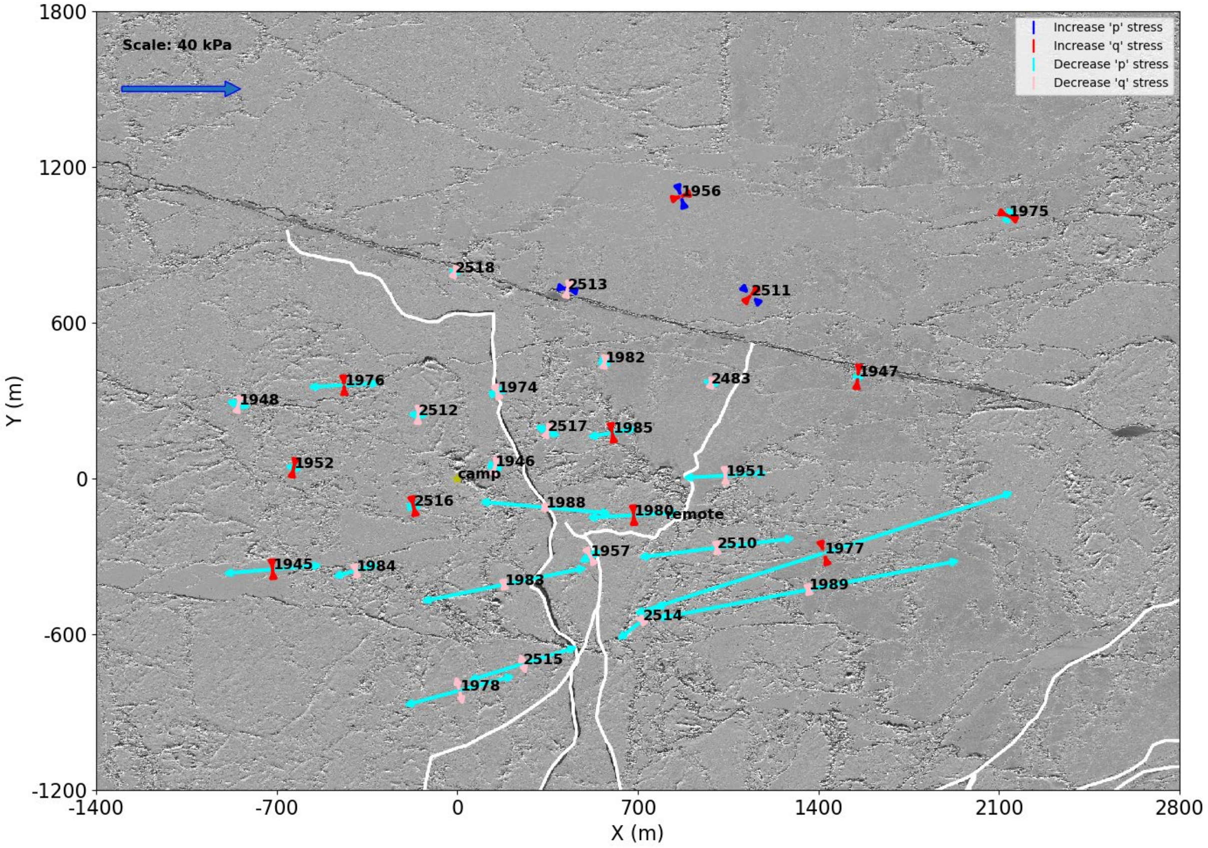

Figure 29. Stress change from 16:43 to 16:50, 15 March.

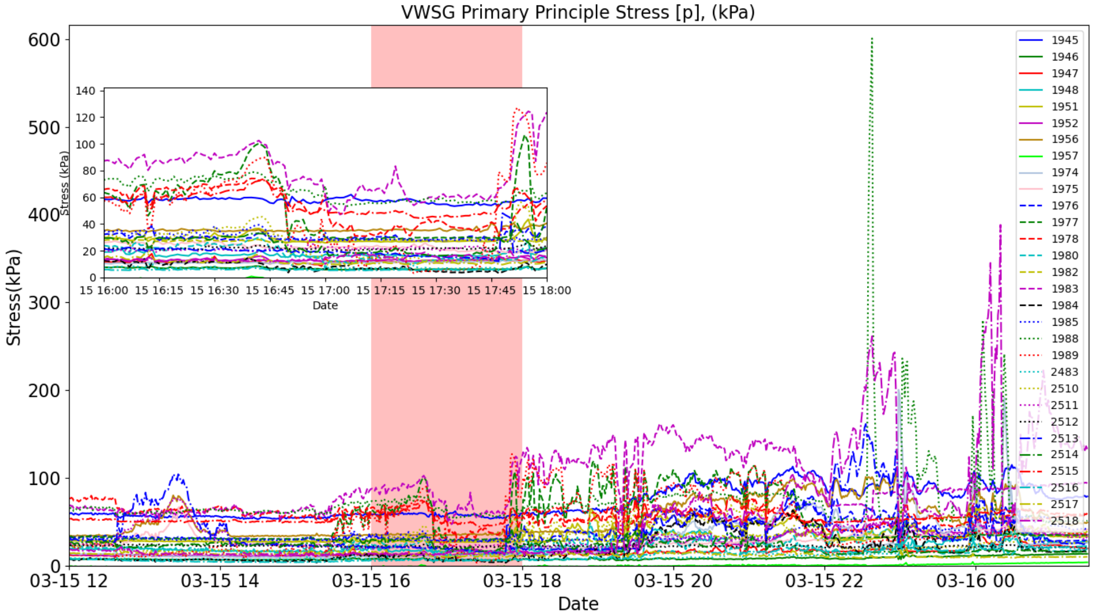

Figure 30. Timeseries stress record of FP 2 with an inset of the FP 2 initial fracture

Stress is largely unchanged after this event until 17:16 when the southern region of the stress array is reloaded. This is followed by a period where we see high-magnitude, high-frequency stress events alternating between sensors 1976, 1988, and 2518 along the N-S fault separating the Main Camp from the East Camp. Each of these sensors were located on or near asperities that were contact points between local floes. The behavior is particularly notable in a large loading and subsequent unloading of the 1988 sensor over a 10-minute period starting at 22:33 seen in the inset plot of figure 32. Starting at 22:31, stress increased to ~600 kPa over a 4-minute period. During this time the stress is oriented nearly parallel to the crack and towards Camp Central 7, which we believe to have caused this load pattern. Local movement between floes was recorded by the LSO during this time (Figure 33). We speculate that Camp Central 8 collided with Camp Central 7 to the south, causing a compressive stress pathway running parallel to the crack. The LKF separating Camp North from Camp ECF had closed at this time, creating a boundary for compression to occur. During this time the secondary principal stress a mere 3.1 kPa, indicating that minimal stresses were propagating orthogonal to the crack.

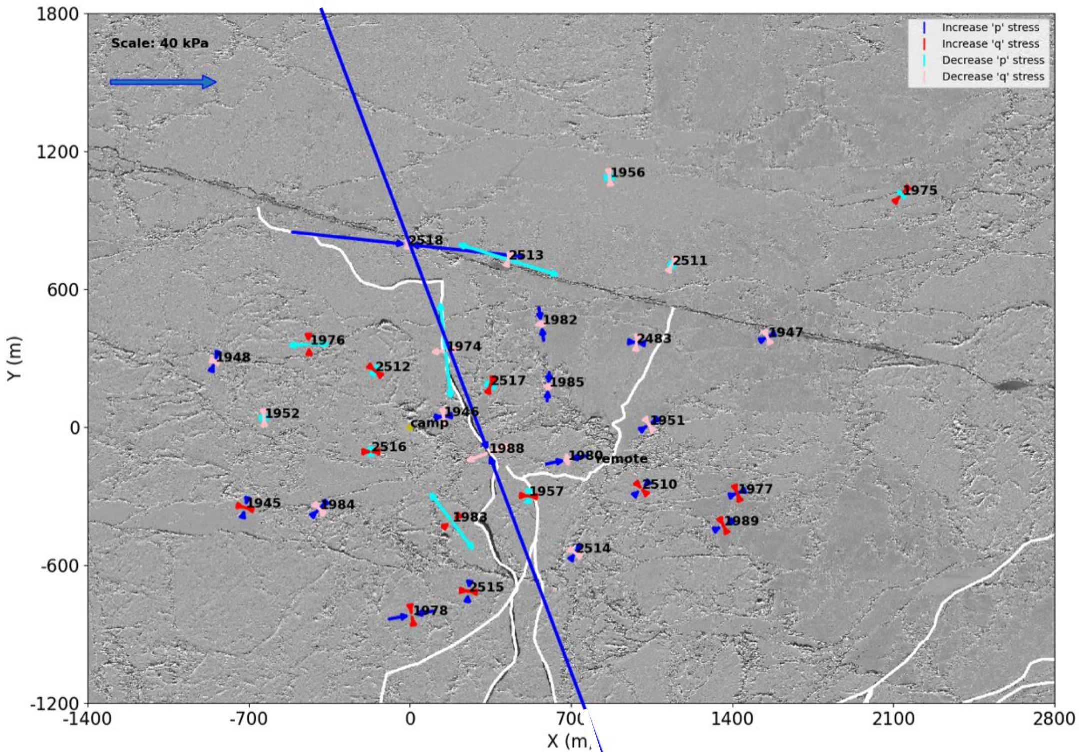

Figure 31. Stress change from 22:33 to 22:37, 15 March.

Over the next hour we saw the rapid unloading of one of the three asperity sensors, followed by the loading of another, maintaining at least one sensor above 150 kPa for 50 minutes.

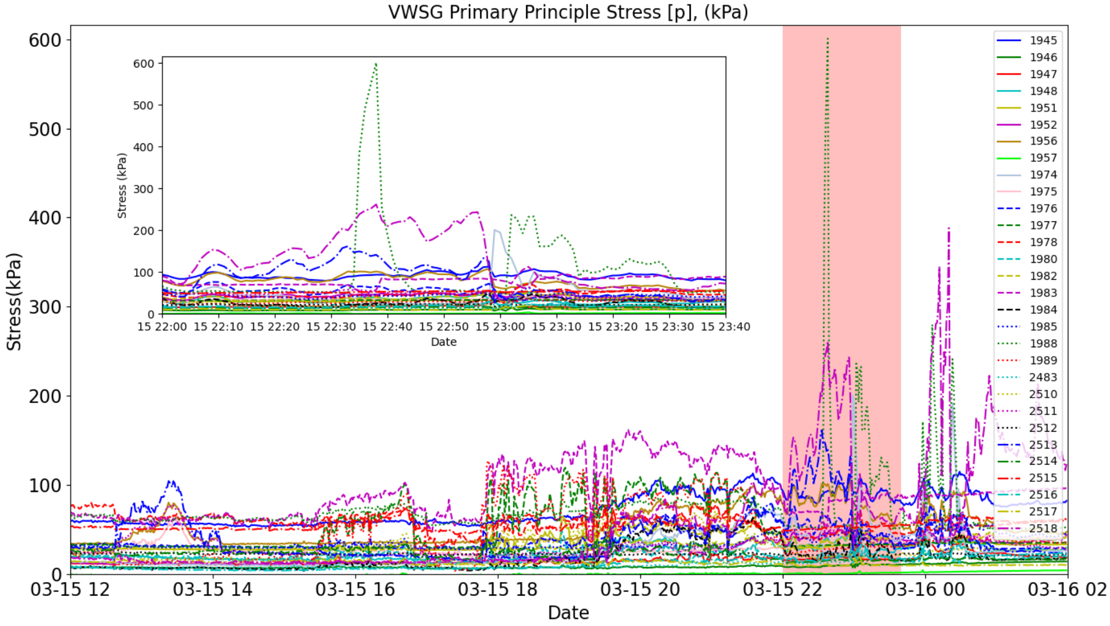

Figure 32. Stress vs. time of FP 2 with an inset of the 22:34-23:40 series of stress events

Strain observations from the LSO help explain what occurred during this period (Figure 33). A line of reflectors running N-S along the fracture experience displacement. Each of these reflectors were located west of the N-S running crack and show that Camp Central 6 moved eastward while Camp Central 7 moved northward.

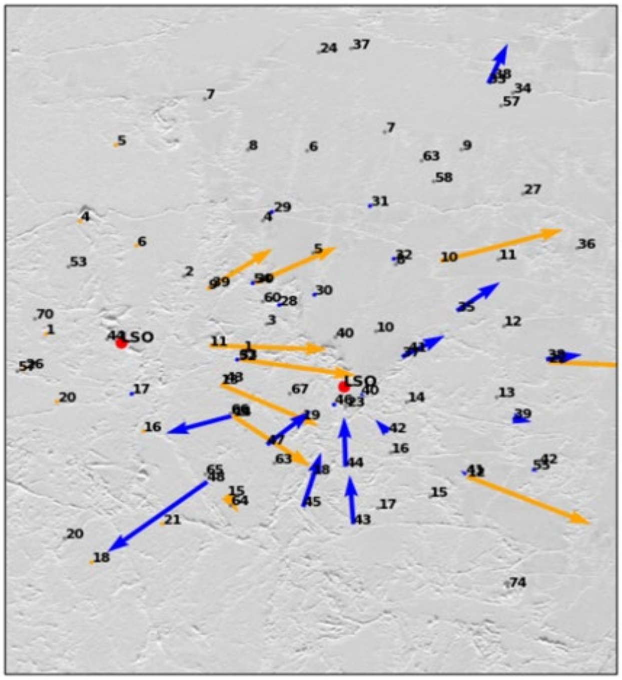

Figure 33. LSO reflector movement from 22:13 to 22:54, 15 March.

This movement appeared to induce shear stress along the eastern Camp Central 1-Camp Central 6 boundary. Following the 22:33-22:43 stress events, the contact geometry shifts at 22:55 to sensor 1974, recording a 174 kPa stress increase over a 4-minute period (Figure 34). Transforming the stress into a coordinate system relative to the crack, we find that the normal stress orthogonal to the crack was 70.6 kPa and the shear stress was 93.6 kPa, indicating a right-lateral compressive shear.

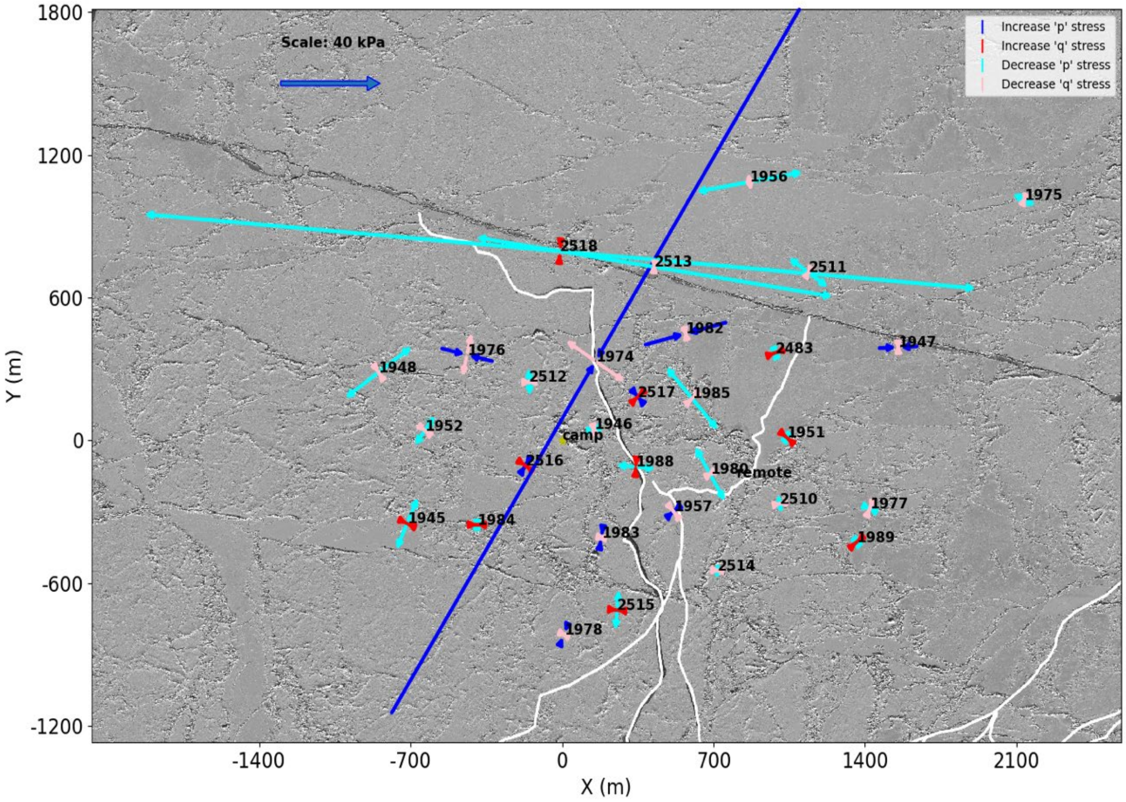

Figure 34. Stress change from 22:55 to 22:59, 15 March

Immediately following this, 1974 unloads and 1988 increases in stress by 182 kPa from 22:59 to 13:05 (Figure 35). The orientation changes at this time to a left-lateral compressive shearing at the 1988 asperity, showing a quickly evolving environment as larger floes reorient the smaller Camp Central 6 and Camp Central 7 floes. The normal stress orthogonal to the crack was found to be 208 kPa, with a corresponding shear stress of -58 kPa. The ice then begins unloading until 16 March when the asperities once again experience alternating high loads through the end of FP 2 at 01:30, 16 March.

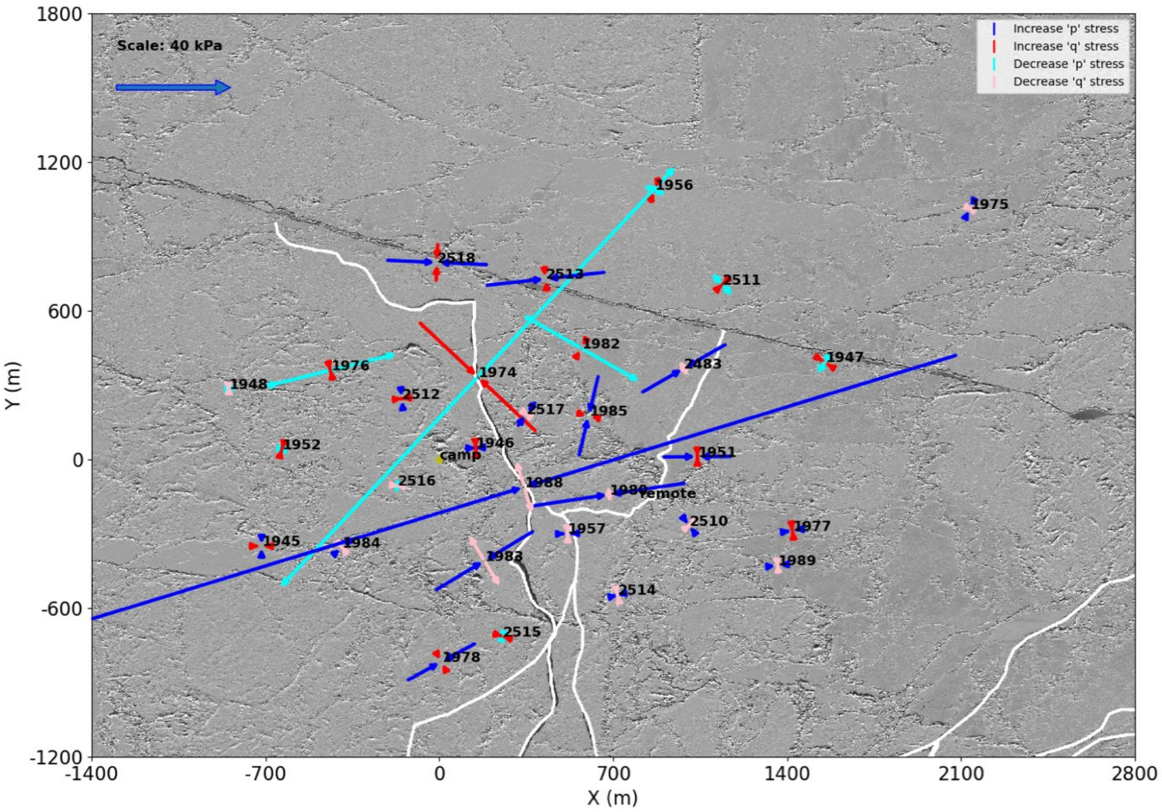

Figure 35. Stress change from 22:59 to 23:03, 15 March

4.3.5. Inter-FP 2: 01:00, 16 March to 01:30, 19 March

Inter-FP 2 takes place during a time of southwestward drift that is pushing the ice against the coast. During this time the ice experiences minimal dynamic stress, containing a 56.52-hour LP. Stress events were mostly isolated to V1988, where the dynamic stress remains active until 04:00, 17 March. Stress fluctuations observed by the array are mostly smooth and gradual, with a diurnal periodicity consistent with thermal stresses until the beginning of DP 3. No fractures were observed within the sensor array during this time.

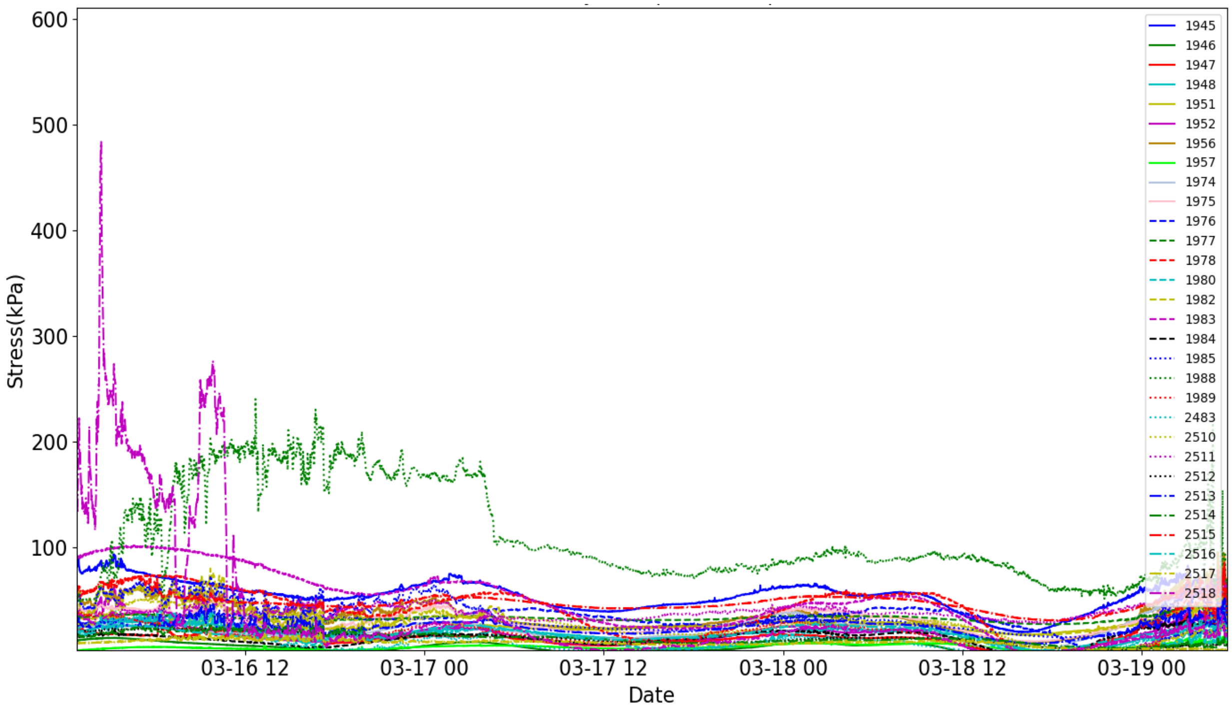

Figure 36. Stress vs. time during Inter-FP 2.

4.3.6. Fracture Period 3: 01:30, 19 March to 06:00, 20 March

Fracture Period 3 consisted of a sustained southwestward drift, resulting in the compaction of the Camp Floe. During this time the Camp East 2-East Floe boundary underwent left-lateral shear, progressively removing the highly fractured ice to the east while placing Camp Central in contact with the broken up Camp South. This resulted in S-N fracture propagation through the array, causing Camp Central to be comprised of 10 individual floes. The stress array observed a S-N dominant stress orientation until the floe broke up around 02:00. Stress decreases and increases occurred uniformly at times, with the largest stress event by power index resulting from a floe-wide decompression event at 17:35, 19 March. The second largest stress event loaded Camp West while relieving Camp Central, East, and North. We observe the contact chain of ice changes rapidly as the fraction of load-bearing ice changed quickly, sometimes on the order of minutes, during this time.

MODIS imagery captures the southward drift and subsequent deformation of the Beaufort Sea ice cover. Large LKFs can be seen to propagate through the pack between 14 March (Figure 37) and 18 March (Figure 38).

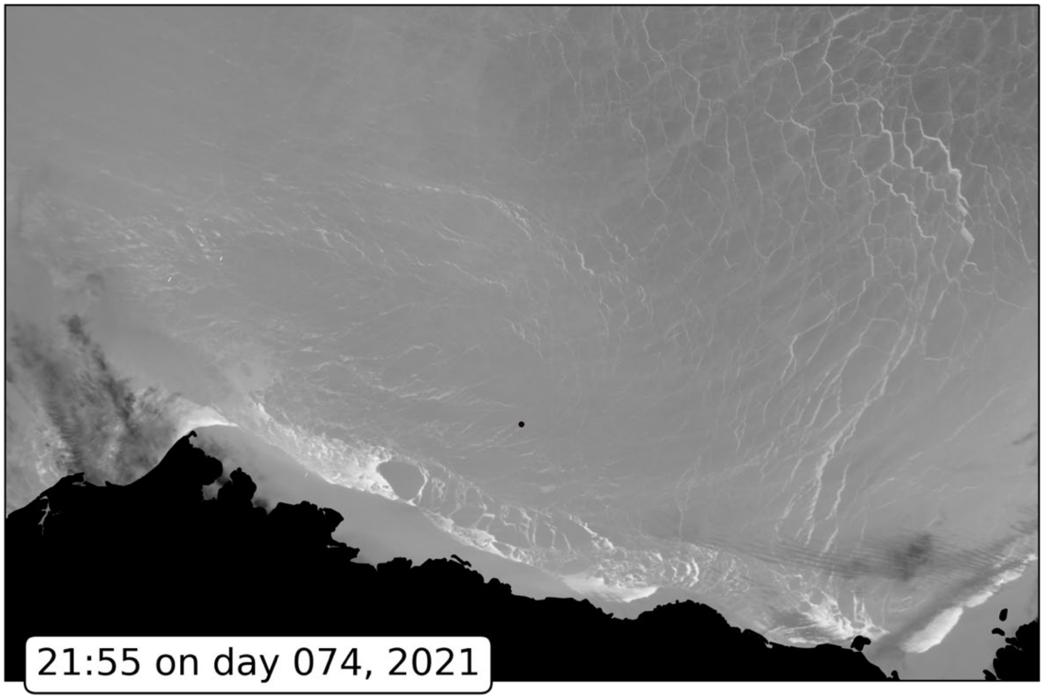

Figure 37 (top). MODIS image of Southern Beaufort Sea on 21:55, 14 March.

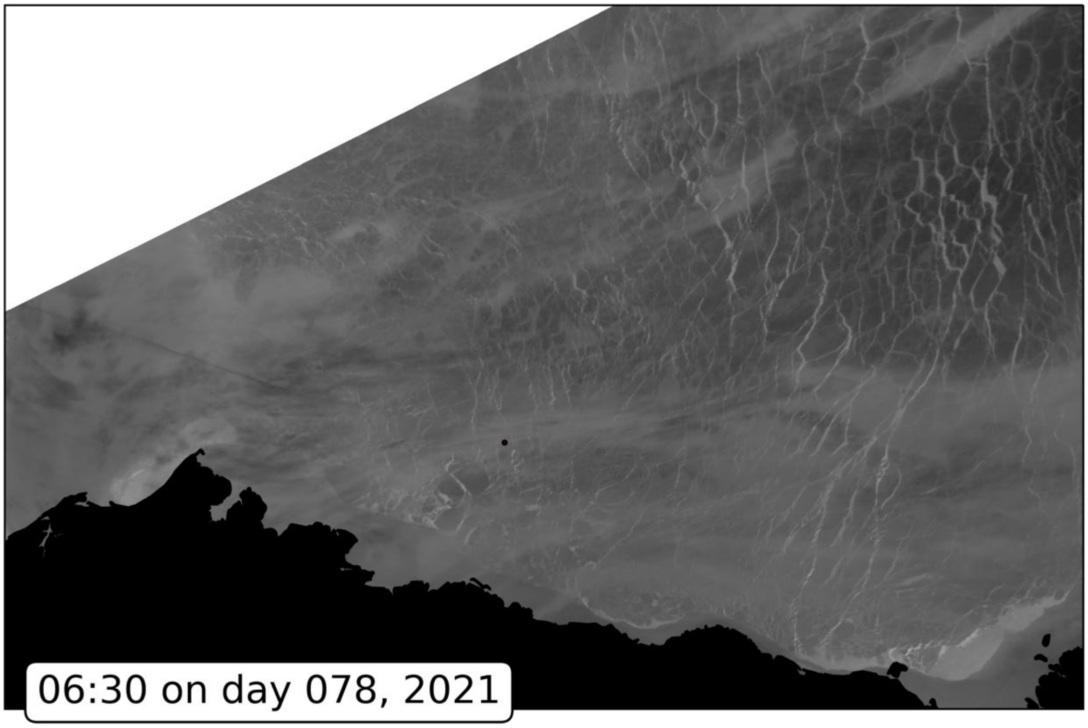

Figure 38 (bottom). MODIS image of Southern Beaufort Sea on 06:30, 18 March.

One of these LKFs appears to extend through the Camp Floe, creating a ~2km-wide shear band to the SE of the stress array. This results in Camp East 2 being broken into smaller floes that connect the East Floe with Camp Central and Camp East at narrow contact points.

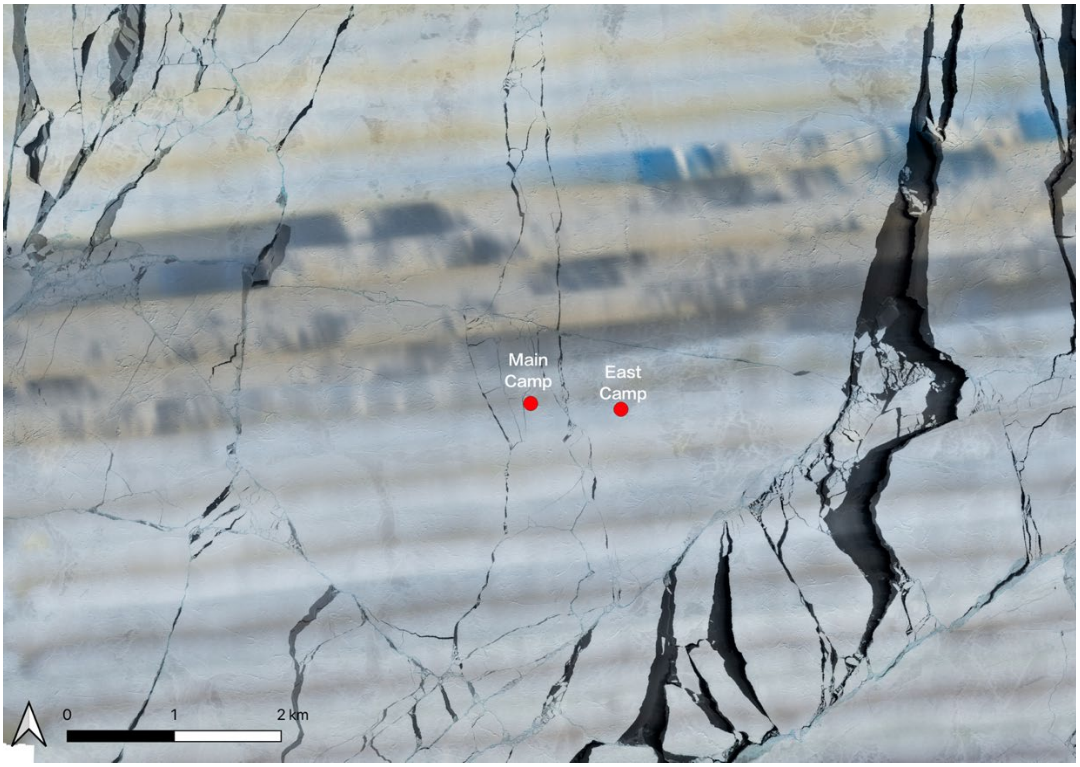

Figure 39. Aerial structure-from-motion image of floe deformation and cracks on 20 March.

The first fracture to propagate through the sensor array during FP3 occurred between 04:08 and 04:14, 19 March (Figure 40). The GPRI recorded this fracture propagating from Camp South through Camp North over a 4-minute period, partially reusing the LKF from FP 2 that separated Main Camp from East Camp. The stress change seen during this period was relatively small as the ice retained much of its load, oriented in the N-S direction.

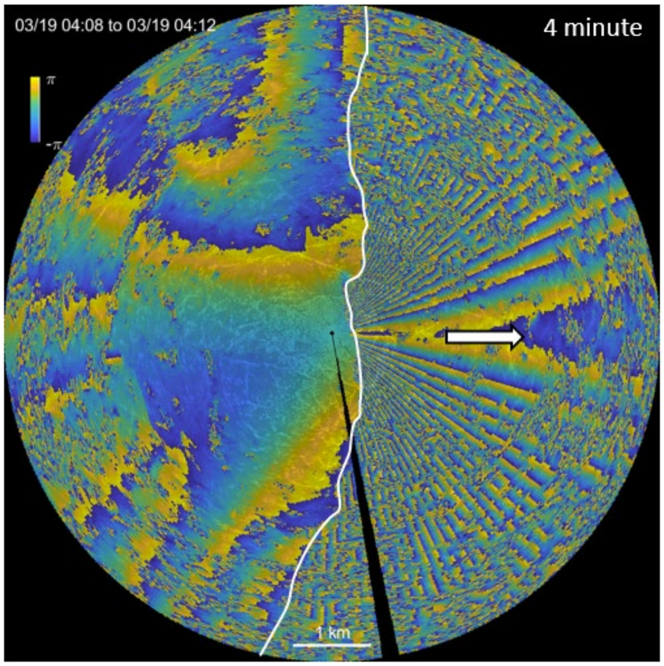

Figure 40. GPRI interferogram calculated from 04:08 to 04:14, 19 March.

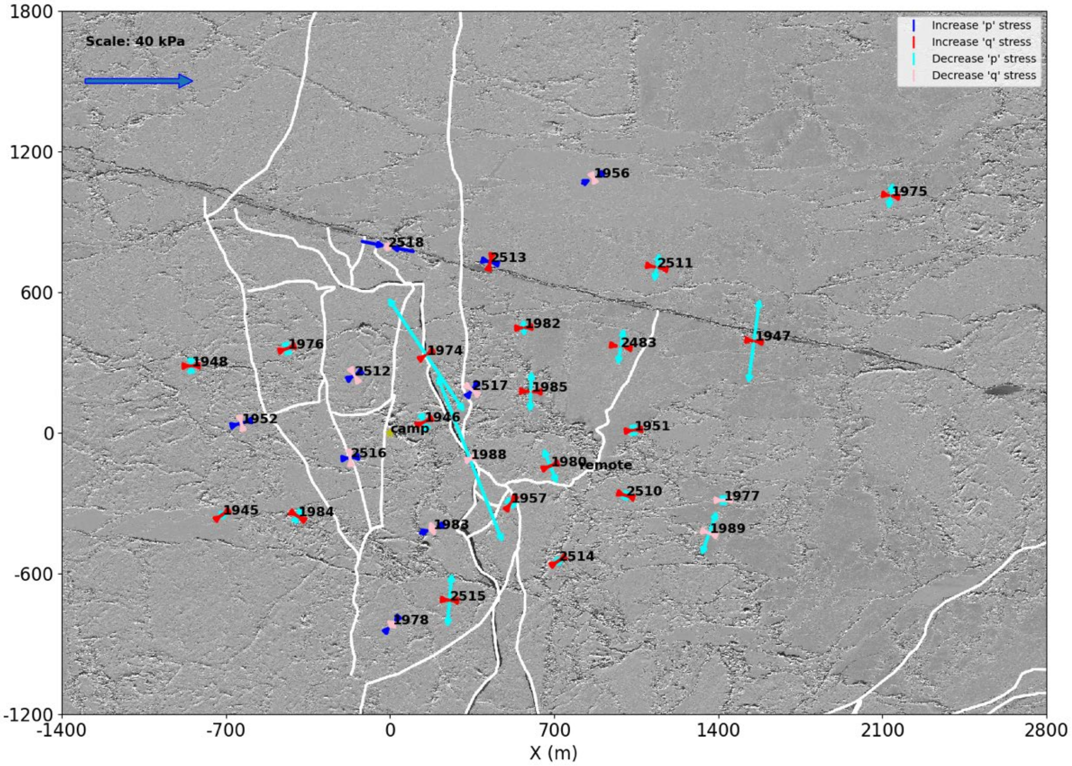

Figure 41. Stress change from 04:09 to 04:10, 19 March

Following this initial fracture, many additional cracks were recorded through the sensor array as the East Floe continues to contact Camp East and Camp South. This culminates in fractures later in the day which were recorded by the SIDEx strain arrays. SIDEx GNSS stations show differential movement beginning around 18:30 (Figure 42).

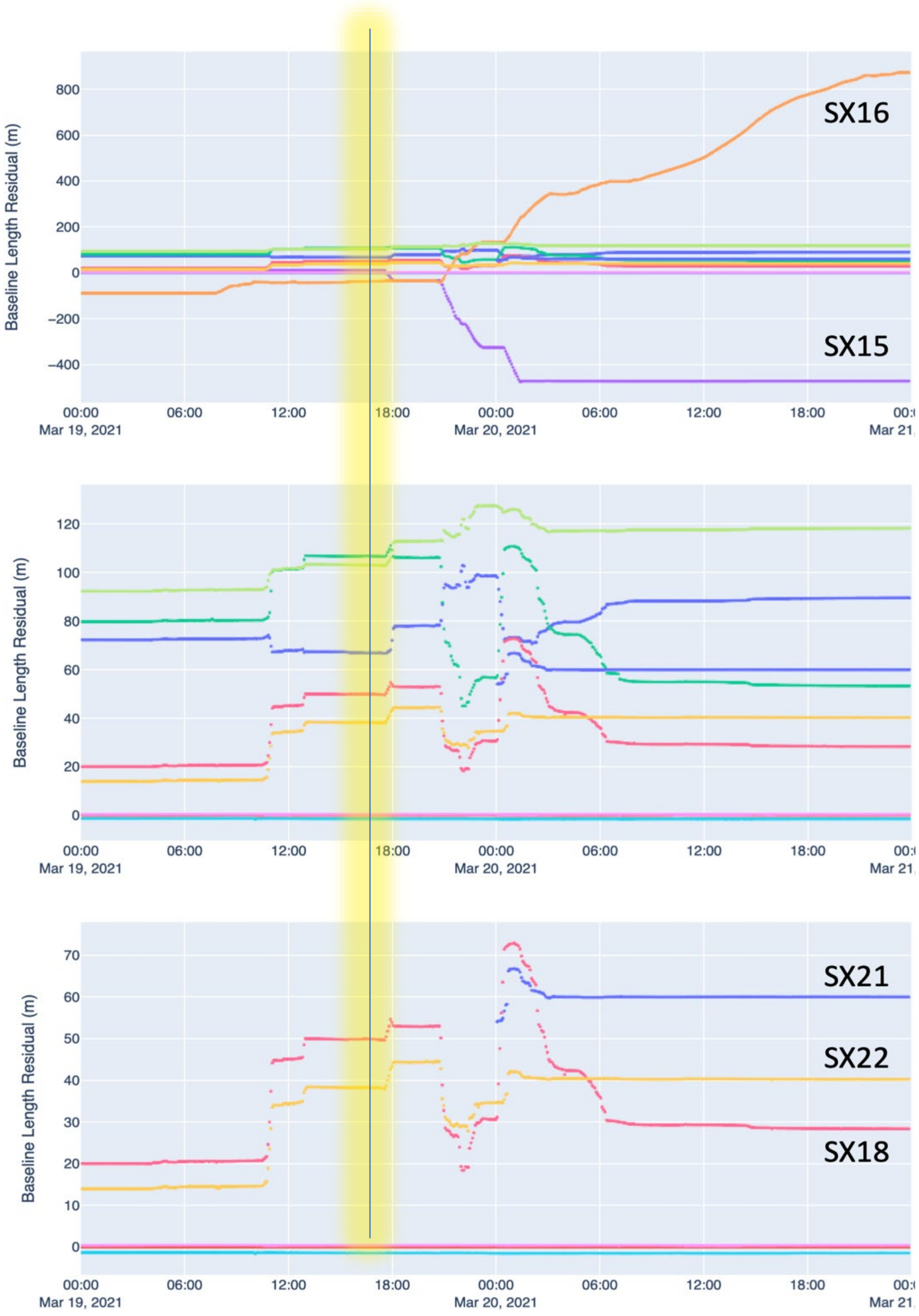

Figure 42. GNSS record of buoy position change during FP 3.

The VWSG array observes decreases in stress that preceded the larger ice movement. At 17:35 a stress event occurred with the highest power index seen across FP 1, FP 2, and FP 3. The event consisted of 23 sensors recording a stress change of over 15 kPa, with a peak drop of 103.14 kPa across the minute. This results in a power index of 81.3, considerably higher than the 4.8 power index of the FP 3 initial fracture. The stress change was mostly oriented in the N-S direction and was seen strongest to the north and east of camp.

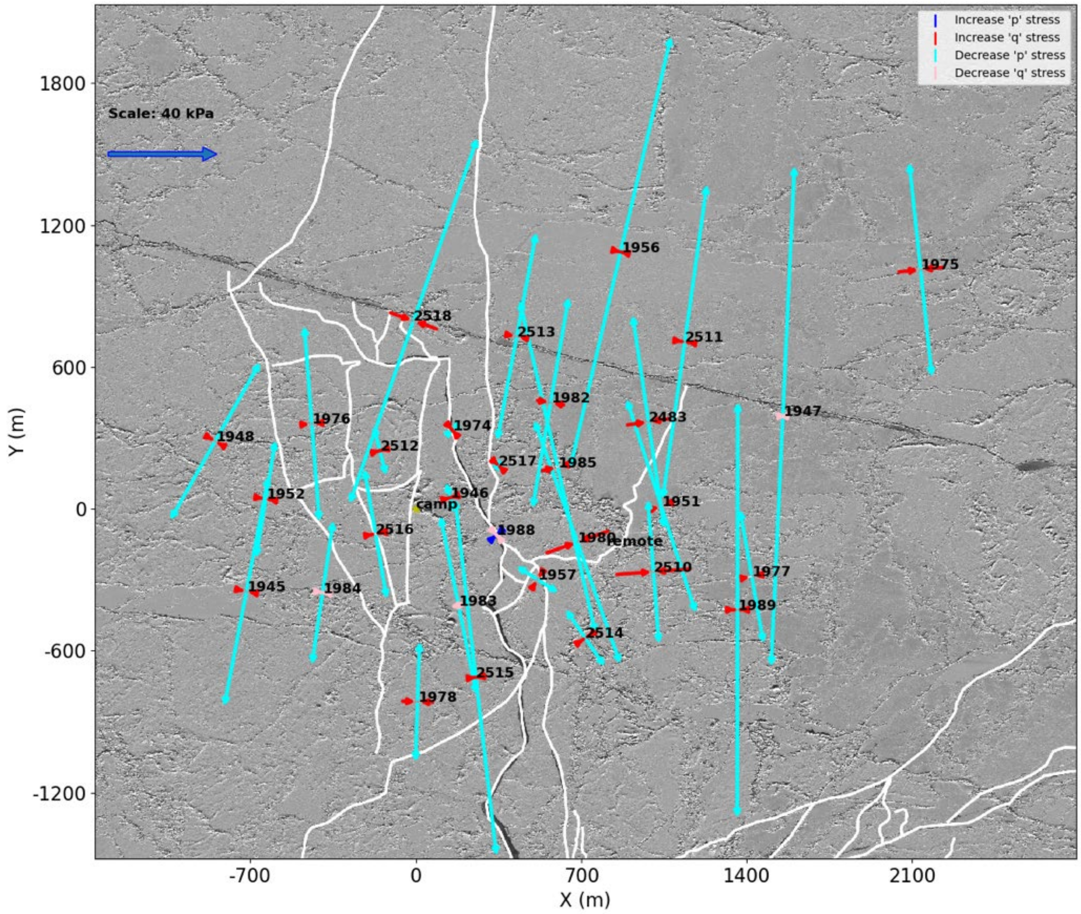

Figure 43. Stress release between 17:35 and 17:36, 19 March.

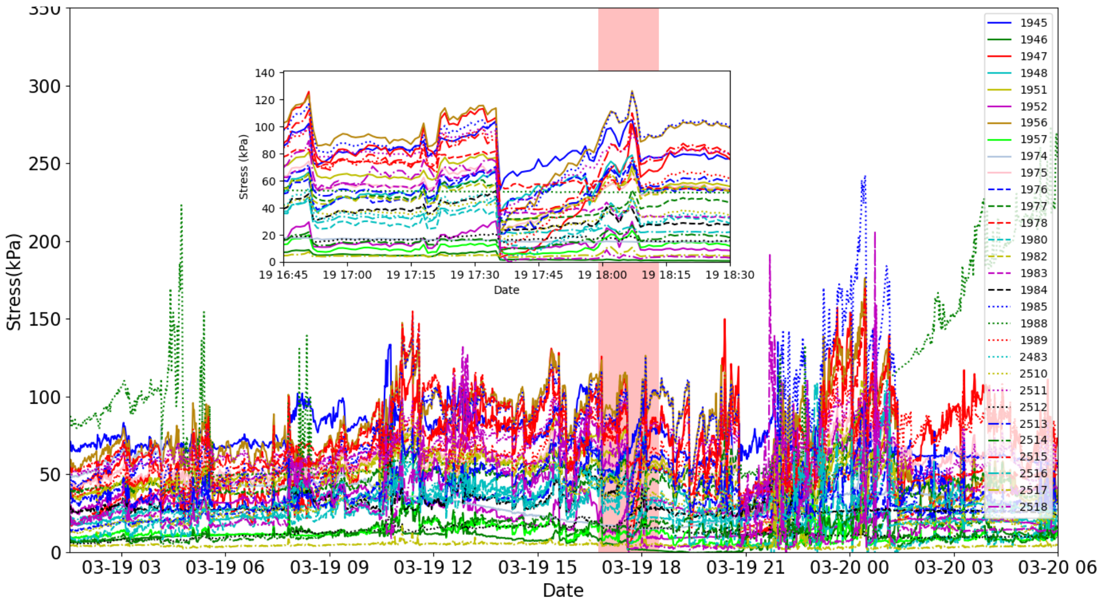

Figure 44. Stress vs. time of FP 3 with an inset around the 17:35 stress event.

The second strongest stress event by power index during FP 3 came at 20:48. Here, Camp Central 6 and 7, Camp East 1, and Camp North 3 decreased in stress, while the rest of Camp Central and Camp West increased in stress. 16 sensors changed by more than 15 kPa, with a peak drop of 113.28 kPa.

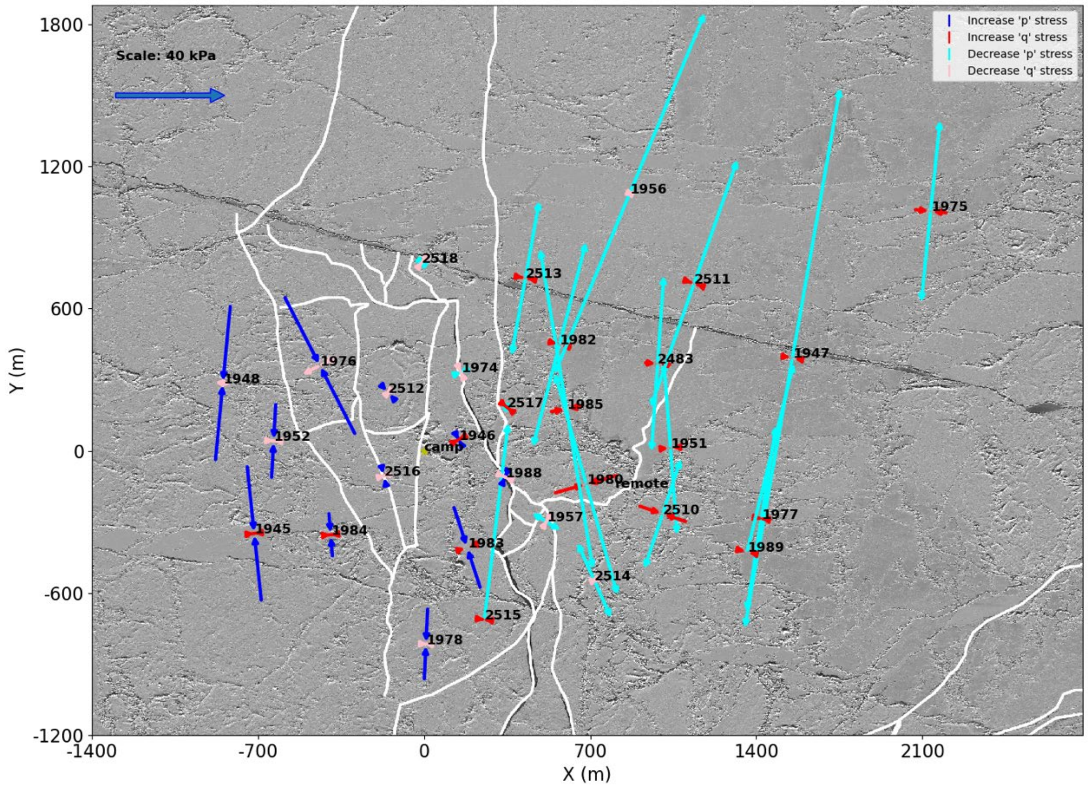

Figure 45. Stress change from 20:48 to 20:49, 19 March

Camp West records a stress increase, Camp Central mostly records a stress increase, and Camp East records a stress decrease during this time. Following the 20:48 stress event, the VWSG array saw a period of low dynamic stresses from 20:50 to 21:39. These events led to the breakup of the Camp Floe and the end of the manned SIDEx operation. The stress sensors were set up to operate remotely until an equipment recovery operation was launched later in April.

4.3.7. Post-FP 3: 06:00, 20 March thru 00:00, 21 April

After FP 3 the ice experienced many stress events and subsequent fractures. This period offers strong candidates for further exploration and should be the subject of future analysis. We have chosen to omit this from our discussion for brevity, and since the ice at this time was fractured to the point that resolving the local deformation will require more time than is available for this thesis.

In summation, the ice post-FP 3 continued its trend of dynamic activity being particularly strong for a couple of days, followed by thermally driven periods where the ice sees minimal dynamic stress. From 06:00, 20 March to around 12:00, 23 March sensor 1988 continues recording a high frequency of stress events relative to the other sensors. The rest of the ice maintains a mostly thermal signal up until 00:00, 22 March when ice-motion driven stresses appear to increase.

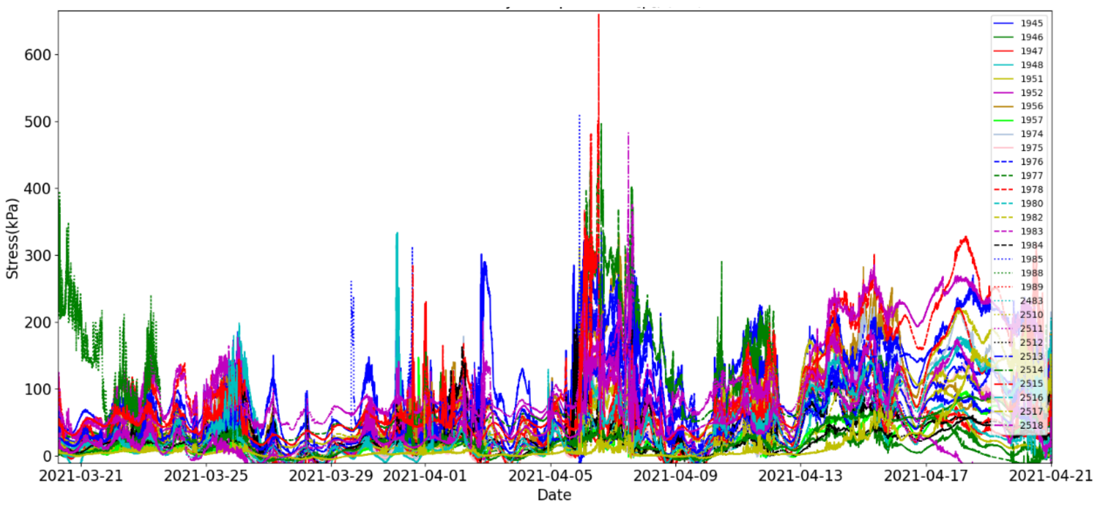

Figure 46. Stress vs. time from the end of FP 3 to the conclusion of the experiment on 21 April.

A particularly strong DP occurs from 10:00, 05 April to 03:00, 08 April (Figure 46). Here, we observe that the range of stress during the 08 April LP (225 kPa) more than doubles from the 05 April LP (105 kPa), indicating an increase in residual stresses. This spread continues to widen through the rest of the campaign to over 300 kPa on 18 April. In future studies of this period, it will be important to resolve if this is an artificial result of sensor drift or if it is reflective of the ice environment, which is not undertaken in this thesis.

5. Discussion

The three fracture periods analyzed in this study provide unique case studies of how contact geometry between floes is consistent with the stress state of ice. An important finding is that the fraction of sea ice loaded during any given time is highly variable and can rapidly alternate between contact points. We suggest that this result can be used to improve the current model representation of sea ice dynamics through refining how ice strength is parameterized. Continuum models seek to represent regional-scale ice deformation and stress as a bulk process, representing brittle failure and relative floe movement as aggregated nonphysical abstractions [2], [28]. These models are explicitly noted by the authors to not represent the scale of our study; they are designed to model processes much larger than our own. Additionally, new continuum models have been created that provide different parameterizations of ice failure and strength [29]–[32], seeking to better conform models to observations. We seek to contribute to these sea ice modeling efforts through our analysis of contact geometry-dependent sea ice stress and failure.

Models typically account for the observed difference in failure strength between ice in the field and in the laboratory by assigning a lower ice strength to the modeled environment. We observe that our SIDEx floe did not always behave as a continuum, often loading only a fraction of the floe. FP 3 shows this explicitly. During the 17:35, 19

March stress event the entire floe experienced a ~N-S decompression in stress, displaying uniform behavior over the 4.5km^2 area. Later, during the 20:48 stress event, ice to the west of a fracture experienced compression while ice to the east decompressed, both of which were approximately oriented N-S. It appears that the strength of an ice floe is related to the proportion of its area that is in contact with another body and what the movement between those two are, which might be leveraged for refining parameterization.

We also present further evidence of a “hardening” process occurring during FP 1, similar to findings at the regional scale [15], [18]. While consisting of a different mechanism than regional-scale hardening, where ice contact between ice floes is treated as an overall hardening of the abstracted pack, the “strain hardening” of a single floe displays similar behavior. A quickly fluctuating signal superimposed over an increasing signal reveals weak ice is being removed and stronger ice is taking the load. Such behavior has never been reported and linked to local deformation on the scale of ice floes. During FP 1 the Camp North floe rotated, forcing a narrow contact point to collide with the East Floe. The “weak ice” in our case was not FYI, as has been speculated in past studies. Rather, both MYI and FYI ice fractured at the narrow point (flyover by Polashenski and Mahoney). We recall that any material loaded beyond its yield strength will fail. During the floe rotation, even thick MYI experienced failure because a high load was applied to the entire first layer of ice. The failure of this layer of ice, and subsequent layers later, comprised the high-frequency component of the stress signal. The next layer of ice loaded was broader and could sustain a higher force as it provided a larger area.

This permitted the floe to increase in stress, resulting in the progressively increasing stress signal.

Rapid stress attenuation, similar to the results found at CEAREx [12], was observed during SIDEx, particularly during FP 2. Our data appear to support the hypothesis that the difference between SIMI and CEAREx stress attenuation results was contact geometry [15]. At SIDEx the highest magnitude stresses came along the fracture separating Camp Central 1 from Camp Central 5 and 6. We observe that sensors experiencing the high-magnitude events are located at asperities along the boundary, creating a narrow contact geometry between floes that results in a highly localized load. None of the floe-floe interactions at camp were seen to cause stress propagation past the first layer of sensors. We speculate that this could be due to a lack of force by the colliding floe. During FP 1 and FP 3, far field stresses propagate through the sensing array due to large scale ice motion that caused extensive fracturing elsewhere in the region. During FP 2, the primary stress events analyzed were from local floe interaction. Our data support the hypothesis that contact geometry influences the degree of stress attenuation from a floe edge in sea ice.

6. Conclusion

Through this study we seek to fill a knowledge gap in the mechanical behavior of sea ice at the meter-to-kilometer (m-km) scale; the scale of ice floes. Technological limitations have inhibited contemporaneous stress-strain-fracture observations at this scale in the past. Models must currently use the fracture mechanics derived from experiments at different scales to approximate kinematic interactions since observations are lacking.

The Sea Ice Dynamics Experiment (SIDEx) was run from February 2022 to April 2022 to collect these data using stress sensors, radar and laser interferometers, and satellite imagery of various spatial and temporal resolutions. We use the stress data from the experiment, collected using 31 Vibrating Wire Stress Gages (VWSG) installed over a 4.5 km^2 area, to describe the stress state before and after known fractures. 3 case studies of fracture events between 14 March 2021 and 24 March 2021 are presented.

We find that contact geometry and floe-floe interactions drive ice fracture during each of the 3 fracture periods (FP) presented. During FP 1 and FP 3, far-field stresses are exerted on the Camp floe from contact points many kilometers away. The orientation of these stresses match known contact points between the Camp Floe and surrounding neighbors, and regional deformation can be used to explain the stress state. For FP 2, local deformation measurements are used to explain the high-frequency, high-magnitude stresses that occur near a crack that propagated through the array on 15 March. Stresses are shown to be highly localized in this environment and rapidly attenuate from the floe edges. We observe shear occurring on a local scale, following a peak compressive stress of over 600 kPa at a different location along the fracture, showing how local ice movement creates various loading conditions within minutes. In all cases, we observe contact geometry to be a critical component of ice failure and mechanical behavior at the scale of ice floes.

References

[1] J. Stroeve and D. Notz, “Changing state of Arctic sea ice across all seasons,” *ERL*, vol. 13, no. 10, p. 103001, 2018, doi: 10.1088/1748-9326/aade56.

[2] W. D. Hibler, “A Dynamic Thermodynamic Sea Ice Model,” *Journal of Physical Oceanography*, vol. 9, no. 4, pp. 815–846, Jul. 1979, doi: 10.1175/1520-0485(1979)009<0815:ADTSIM>2.0.CO;2.

[3] J. Weiss, E. M. Schulson, and H. L. Stern, “Sea ice rheology from in-situ, satellite and laboratory observations: Fracture and friction,” *Earth and Planetary Science Letters*, vol. 255, no. 1, pp. 1–8, Mar. 2007, doi: 10.1016/j.epsl.2006.11.033.

[4] P. R. Sammonds, D. C. Hatton, and D. L. Feltham, “Micromechanics of sea ice frictional slip from test basin scale experiments | Philosophical Transactions of the Royal Society A: Mathematical, Physical and Engineering Sciences,” 2017. https://royalsocietypublishing.org/doi/10.1098/rsta.2015.0354 (accessed Oct. 12, 2021).

[5] E. M. Schulson and Paul. Duval, *Creep and fracture of ice*. Cambridge, UK ; Cambridge University Press, 2009.

[6] J. Weiss, *Drift, Deformation, and Fracture of Sea Ice: A Perspective Across Scales*, vol. 83. Springer Dordrecht, 2013.

[7] R. J. Evans and N. Untersteiner, “Thermal cracks in floating ice sheets,” *Journal of Geophysical Research (1896-1977)*, vol. 76, no. 3, pp. 694–703, Jan. 1971, doi: 10.1029/JC076i003p00694.

[8] Z. P. Bažant, “Large-scale thermal bending fracture of sea ice plates,” *Journal of Geophysical Research: Oceans*, vol. 97, no. C11, pp. 17739–17751, 1992, doi: 10.1029/92JC00816.

[9] E. M. Schulson, “Compressive shear faults within arctic sea ice: Fracture on scales large and small,” *Journal of Geophysical Research: Oceans*, vol. 109, no. C7, pp. C07016-n/a, 2004, doi: 10.1029/2003JC002108.

[10] G. F. N. Cox and J. B. Johnson, “Stress measurements in ice,” COLD REGIONS RESEARCH AND ENGINEERING LABORATORY, HANOVER NH, 1983, p. 37.

[11] J. B. Johnson, G. F. N. Cox, and W. B. Tucker, “Kadluk ice stress measurement program,” presented at the 8th International Conference on Port and Ocean Engineering Under Arctic Conditions, Dan. Hydraul. Inst., Horsholm, Denmark, 1985.

[12] W. B. Tucker and D. K. Perovich, "Stress measurements in drifting pack ice," *Cold regions science and technology*, vol. 20, no. 2, pp. 119–139, 1992, doi: 10.1016/0165-232X(92)90012-J.

[13] G. Comfort and R. Ritch, "Field measurements of pack ice stresses," in *9th Int. Conf. of Offshore Mechanics and Arctic Engineering*, Houston, Texas, 1990, vol. Book 10296F, pp. 177–181.

[14] M. D. Coon, G. S. Knoke, D. C. Echert, and H. L. Stern, "Contemporaneous field measurements of pack ice stress and ice strain measurements from SAR imagery," in *OCEANS '93*, 1993, vol. 3, pp. III31–III36. doi: 10.1109/OCEANS.1993.326154.

[15] J. A. Richter-Menge and B. C. Elder, "Characteristics of pack ice stress in the Alaskan Beaufort Sea," *Journal of Geophysical Research: Oceans*, vol. 103, no. C10, pp. 21817–21829, 1998, doi: 10.1029/98JC01261.

[16] R. M. W. Frederking and E. Evgin, "Analysis of stress distribution in an ice floe," in *Proceedings of the Ninth International Conference on Offshore Mechanics and Arctic Engineering*, New York, 1990, vol. 4, pp. 83–87.

[17] J. E. Overland, S. L. McNutt, S. Salo, J. E. Groves, and S. Li, "Sea ice as a granular plastic," *Journal of Geophysical Research*, no. 103, p. 21,845-21,867, 1998a.

[18] J. A. Richter-Menge, S. L. McNutt, J. E. Overland, and R. Kwok, "Relating arctic pack ice stress and deformation under winter conditions," *Journal of Geophysical Research*, vol. 107, no. C10, p. SHE 15-1, 2002, doi: 10.1029/2000JC000477.

[19] M. A. Hopkins, "In the mesoscale interaction of lead ice and floes," *Journal of Geophysical Research*, no. 101(C8), p. 18,315-18,326, 1996.

[20] "Biaxial Stressmeters (VW)," *GEOKON*. https://www.geokon.com/4350 (accessed Mar. 30, 2022).

[21] Y. Hata and L. Tremblay, "Anisotropic internal thermal stress in sea ice from the Canadian Arctic Archipelago," 2015, doi: 10.1002/2015JC010819.

[22] J. Parno, C. M. Polashenski, M. Parno, T. Nelsen, A. R. Mahoney, and A. Song, "Observations of Stress-Strain in Drifting Sea Ice at Floe Scale," *Earth and Space Science Open Archive*, Jul. 27, 2021. http://www.essoar.org/doi/10.1002/essoar.10507623.1 (accessed Oct. 11, 2021).

[23] "CRVW3 - 3-Channel Vibrating-Wire Datalogger." https://www.campbellsci.com/crvw3 (accessed Mar. 31, 2022).

[24] E. M. Schulson, A. L. Fortt, D. Iliescu, and C. E. Renshaw, "Failure envelope of first-year Arctic sea ice: The role of friction in compressive fracture," *Journal of*

Geophysical Research, vol. 111, no. C11, p. C11S25-n/a, 2006, doi: 10.1029/2005JC003235.

[25] "Leica Nova TM50 – To effectively manage & monitor structures." https://leica-geosystems.com/en-US/products/total-stations/robotic-total-stations/leica-nova-tm50 (accessed Mar. 31, 2022).

[26] F. ID, "GPRI-II-2 Radar Interferometer Operational Description GAMMA Remote Sensing and Consulting AG," *FCC ID*. https://fccid.io/Y3Z-GPRI-II-2/Operational-Description/Operational-Description-2386212 (accessed Mar. 31, 2022).

[27] P. Elosegui *et al.*, "High-precision GPS autonomous platforms for sea ice dynamics and physical oceanography," presented at the AGU Fall Meeting 2012, San Francisco, California, Dec. 2012.

[28] M. D. Coon, S. A. Maykut, R. S. Pritchard, D. A. Rothrock, and A. S. Thorndike, "Modeling the pack-ice as an elastic-plastic material," AIDJEX Bulletin Numerical Modeling Report 24.

[29] L. Girard, S. Bouillon, J. Weiss, D. Amitrano, T. Fichefet, and V. Legat, "A new modeling framework for sea ice mechanics based on elasto brittle rheology," *Annals of Glaciology*, no. 52(57).

[30] V. Dansereau, J. Weiss, P. Saramito, and P. Lattes, "A Maxwell elasto-brittle rheology for sea ice modelling," *The Cryosphere*, no. 10, pp. 1339–1359, 2016.

[31] H. L. Schreyer, D. L. Sulsky, L. B. Munday, M. D. Coon, and R. Kwok, "Elastic-decohesive constitutive model fro sea ice," *Journal of Geophysical Research: Oceans*, no. 111(C11), 2006.

[32] M. Tsamados, D. L. Feltham, and A. V. Wilchinsky, "Impact of a new anisotropic rheology on simulations of Arctic sea ice," *Journal of Geophysical Research: Oceans*, no. 118(1), pp. 91–107, 2013.